Nano Today 55 (2024) 102156

Contents lists available at ScienceDirect

Nano Today

journal homepage: www.elsevier.com/locate/nanotoday

# A metalloprotein nanoparticle scaffold co-delivers antigens and adjuvants with metal-enhanced STING activation for vaccination preventing viral infections

Jiexin Li [a], Qian Qiu [a], He Ren [a], Jingyu Zhang [a], Chen Zhang [a], Gengqi Liu [a], Boyang Sun [a], Bin Zheng [b], Jonathan F. Lovell [c], Yumiao Zhang [a,*]

[a] School of Chemical Engineering and Technology, Key Laboratory of Systems Bioengineering (Ministry of Education), Frontiers Science Center for Synthetic Biology (Ministry of Education), Tianjin University, Tianjin 300350, PR China
[b] Academy of Medical Engineering and Translational Medicine, Tianjin Key Laboratory of Brain Science and Neural Engineering, Tianjin University, 92 Weijin Road, Nankai District, Tianjin 300072, PR China
[c] Department of Biomedical Engineering, The State University of New York at Buffalo, Buffalo, NY 14260, United States

ARTICLE INFO

*Keywords:*
Lyophilized nanovaccine
Metalloprotein
Metalloimmunotherapy
CGAS-STING pathway
Virus prevention

ABSTRACT

Co-delivery of antigens and adjuvants in a nanoparticle format could be beneficial for subunit vaccine development. Herein, we develop a nanovaccine comprising **la**ctoferrin-**M**n-**P**EG-di**A**BZI-2-antigen, termed LaMP-A-antigen. Featuring a metalloprotein core, LaMP securely localizes manganese (Mn) in confined spaces formed by lactoferrin-PEG conjugates. LaMP efficiently coordinates imidazole-containing adjuvants (diABZI-2), yielding LaMP-A, which is subsequently functionalized by numerous his-tagged viral-derived antigenic proteins or peptides by simple admixture. Compared to regular metal chelation, LaMP-A-antigen is more physiologically stable and can be lyophilized and stored at room temperature without change in physical and immunological properties for months. Following screening of ten common metal ions, manganese and cobalt are found to enhance the adjuvant effect of diABZI-2 by activation of stimulator of interferon genes (STING). In particular, $Mn^{2+}$ achieves a 39-fold adjuvant dose sparing effect. When the SARS-CoV-2 receptor-binding domain (RBD) is used as a model antigen, immunization with LaMP-A-RBD elicits strong mucosal, humoral and cellular immunity. Following a single intranasal administration of LaMP-A-RBD in hamsters, antigen-specific T cells as well as natural killer (NK) cells are induced, along with RBD-specific IgG and secretory IgA (sIgA), leading to rapid neutralization in a reporter pseudovirus challenge. Thus, the LaMP-A system represents a novel vaccine adjuvant system that displays antigens, and exploits metalloimmune responses via the cGAS-STING pathway to improve vaccine immunogenicity.

## Introduction

Vaccines represent a central public health policy for controlling numerous infectious diseases [1–4]. Among them, subunit vaccines are advantageous owing to a high level of safety, precise targeting of antigens of interest, and safe manufacture [5,6]. Subunit vaccines generally comprise antigens and adjuvants to stimulate effective and durable immune responses [7,8]. As such, rational design of new subunit vaccines co-delivering different functional antigens and adjuvants to larger scaffolds has been a research focus [9]. However, development of vaccines by a straightforward antigen and adjuvant attachment method for efficacious and stable formulations in physiological settings has been challenging.

Methods for incorporating antigens and adjuvants into nanovaccines include encapsulation in nanoparticles or adsorption on surfaces [10–12]. However, hydrophilic antigens and adjuvants can suffer from low encapsulation efficiency and poor stability, leading to premature release [13,14]. Covalent conjugation chemistry offers a wide range of strategies [15–17] such as reacting antigens with amine or thiol groups to nanoparticles with maleimide, succinimidyl ester, and carboximide-activated carboxylic acid [18–20]. In spite of high yields achieved by chemical conjugation, the problem of impaired efficacy due to chemical structure change and the need for chemical reactions arises [21,22]. Moreover, covalent coupling may fail to release the pristine

* Corresponding author.
*E-mail address:* ymzhang88@tju.edu.cn (Y. Zhang).

https://doi.org/10.1016/j.nantod.2024.102156
Received 17 August 2023; Received in revised form 20 December 2023; Accepted 3 January 2024
Available online 19 January 2024

antigens and adjuvants in immune cells, giving rise to impairment of immunogenicity due to alteration of chemical structures [23,24]. Coupling antigens and adjuvants to the lipid backbone in organic solvents has also been pursued [25,26], but this method is only suitable for small immunogenic peptides, but not for proteins that become permanently denatured in organic solvents [27,28]. An alternative strategy that avoids these limitations is the non-covalent approach by coordinating poly-histidine tag (his-tag)- containing antigenic polypeptides to metal-based scaffolds which sometimes suffer from limitations such as physiological instability [29,30]. Meanwhile, emerging vaccines approaches that address these problems were also developed for treatment of malaria, cancers and coronavirus by generating strong cellular immune responses. For example, coordination of metal ions to his-tagged antigenic peptides (cobalt-porphyrin liposome vaccine [31,32], coordination of metal ions to STING agonists (cyclic dinucleotides (CDA), and aminobenzimidazoles (ABZI)) with imidazole groups (Mn-histidine liposome vaccine [33], Mn-naphthalocyanine micellar system[34].

Under pandemic circumstances, it is urgent to distribute sufficient vaccines around the world including in low- and middle-income countries to trigger global herd immunity [35]. However, the COVID-19 pandemic showed that the cold chain and frozen storage requirements pose a substantial bottleneck to vaccine distribution [36,37]. The physiological stability of subunit vaccines is of importance to guarantee injected vaccines are efficacious [38,39].

Taking the aforementioned points together, we herein introduce an approach to anchor metals on proteins yielding a new metal-based nanovaccine platform by confining manganese (Mn) in a lactoferrin (La)-PEG conjugate nanoreactor. As such, firmly embedded in the metal core of **La**-**M**n-**P**EG (LaMP), Mn provides a coordination scaffold for anchoring imidazole-containing adjuvants (such as ABZI, CDA, diABZI, forming LaMP-A) and diverse his-tagged viral antigens (for coronavirus, influenza A H1N1, herpes simplex virus type 2 (HSV), human immunodeficiency virus (HIV), human papilloma virus (HPV), and hepatitis C virus (HCV)) simply by admixture in water. Using this method, the as-formed vaccine, termed LaMP-A-antigen, remains stable in serum and can be lyophilized for long-term storage at room temperature for months. As an example, LaMP-A-RBD elicited a broad spectrum of metalloimmune response mounted against the SARS-CoV-2 receptor-binding domain (RBD). $Mn^{2+}$ synergistically enhanced the prevention effect of the STING agonist diaminobenzimidazole compound by the activation of cGAS-STING, and induced humoral immunity to produce neutralizing antibodies against SARS-CoV-2. A mucosal immune response was also triggered to produce antigen-specific secretory immunoglobulin A (sIgA) in the lung of immunized hamsters. Antigen-specific T cells and antigen-independent natural killer (NK) cells were activated, resulting in prevention of SARS-CoV-2 infection into lung epithelial cells after a single intranasal administration in a pseudovirus-infection model.

## Results and discussions

### *His-tagged antigen protein binding to protein polymer metal core*

Lactoferrin (La) is considered to be a first-line defense protein, playing an important role in protecting against various microbial infections and preventing systemic inflammation [40]. La also has been reported to show immunomodulatory capability by interferon γ (IFN γ) activation and promotion of antigen-specific T cell generation by DC enhancement [41]. Therefore, we chose La as a template to react with aldehyde-functionalized PEG2000 to generate a protein-polymer conjugate (La-PEG) via a Schiff base reaction. A metal core (**La**-**M**n-**P**EG, termed LaMP) was obtained in situ on the La-PEG conjugate by reducing the metal ion ($Mn^{2+}$) in aqueous solution containing 20% (v/v) methanol (Fig. S1a-c, Supporting information). Presumably, $Mn^{2+}$ first bound to negatively charged amino acid residues on the protein surface, and were subsequently reduced by methanol and reducing amino acid residues in the protein [42,43]. Importantly, La should not be deactivated since the catalytic activity was well preserved after treatment by 20% (v/v) methanol using catalase as a surrogate as shown in Fig. S2. Next, we conjugated imidazole-containing adjuvants by coordinating with metals on the metalloprotein by simply incubation. In this study, a STING agonist diABZI derivative (diABZI-2) was first synthesized, which has enhanced STING activation compared with ABZI we previously reported [34] (Fig. S3-35) and then diABZI-2 and LaMP metal core were admixed in aqueous solution containing 20% (v/v) DMSO, given the hydrophobicity of diABZI-2. The chelation efficiency of diABZI-2 reached about 79.2% at Mn:diABZI-2 = 1:1 (n:n)(Fig. S36a-c).

After obtaining the metalloprotein decorated with diABZI-2 (form LaMP-A), various water-soluble viral antigens could be coordinated further on metalloprotein by admixture in aqueous solution. We screened a series of virus-associated antigenic proteins or peptides including RBD, hemagglutinin (HA), antigen peptides of HIV, HPV, HCV, HSV (Fig. 1a,b). These antigens could also be readily chelated, forming LaMP-A-antigen with an efficiency of about 81.2% at RBD:Mn= 0.5:1 (m:m) (Fig. S36d). Therefore, we chose RBD:Mn= 0.5:1 to formulate vaccines. We found that using this artificial metalloprotein as a coordination scaffold, LaMP-A-antigen exhibited excellent stability in serum and its physical and biological properties were well preserved after lyophilization likely because the metal as coordination scaffold was steadily anchored in a confined space when forming protein-PEG conjugate. We used regular form of coordination nanoparticle as a control by admixing of $Mn^{2+}$, PEGylated diABZI-2 and antigen, termed Mn-A-antigen. These two forms of metal nanovaccines were chelated with various antigens including RBD, HA, antigen peptides of HIV, HPV, HCV, HSV, and then subjected to lyophilization and resuspension in ultrapure water. Subsequently, the size, polydispersity index (PDI), antigen and adjuvant retention and immunological properties of these two formulations were measured. As shown in Fig. 1c-f, compared with the Mn-A-antigen nanovaccine, the size, PDI, antigen and adjuvant content of the reconstituted LaMP-A-antigen did not change significantly. Similarly, after incubation in 20% FBS for 24 h, the contents of antigen and adjuvant and the size of LaMP-A-antigen nanovaccines remained unchanged (Fig. 1g-j). To further assess the immune function of this new metalloprotein-based nanoplatform, we vaccinated mice by intranasal administration of Mn-A-RBD and LaMP-A-antigen and measured the antibody levels of bronchoalveolar lavage fluid (BALF), nasopharyngeal lavage fluid (NPLF), and serum 14 days after vaccination. In stark contrast, LaMP-A-RBD exhibited higher levels of antigen-specific sIgA and immunoglobulin G (IgG) antibodies in BALF, NPLF and serum than that of Mn-A-RBD by 282, 348 and 167 times, respectively (Fig. 1k-n). Other antigens for respiratory and non-respiratory system associated diseases were also investigated. Similarly, compared with Mn-A-antigen, LaMP-A-antigen also induced higher antigen-specific sIgA and IgG antibodies in BALF, NPLF and serum (Fig. 1o,p and Fig. S37a,b). These results demonstrated that LaMP-A-antigen presented a generalized metal nanovaccine platform that could activate effective humoral and mucosal immunity in vivo. Given that SARS-CoV-2 and mutant strains have caused devastating global viral pandemic, resulting in severe global public health crisis, [44,45] our following experiments focus on the antigen RBD to detect the metalloimmune response triggered by LaMP-A-RBD.

### *$Mn^{2+}$ synergistically potentiates STING agonist activity in vitro and in vivo*

Before characterization of LaMP-A-antigen, we first investigated the mechanism how the combination of $Mn^{2+}$ and STING agonist synergistically exerted their adjuvant effect. Previously, we and other research groups demonstrated that metal ions could effectively enhance STING agonist (ABZI) activity and boost interferon-I (IFN-I) response for anti-tumor immunotherapy and IFN-I is a key link between innate immunity and adaptive immunity, activating DC cells and T cells. IFN-I can also activate NK cells and induce NK cells to secrete factors (such as IFN

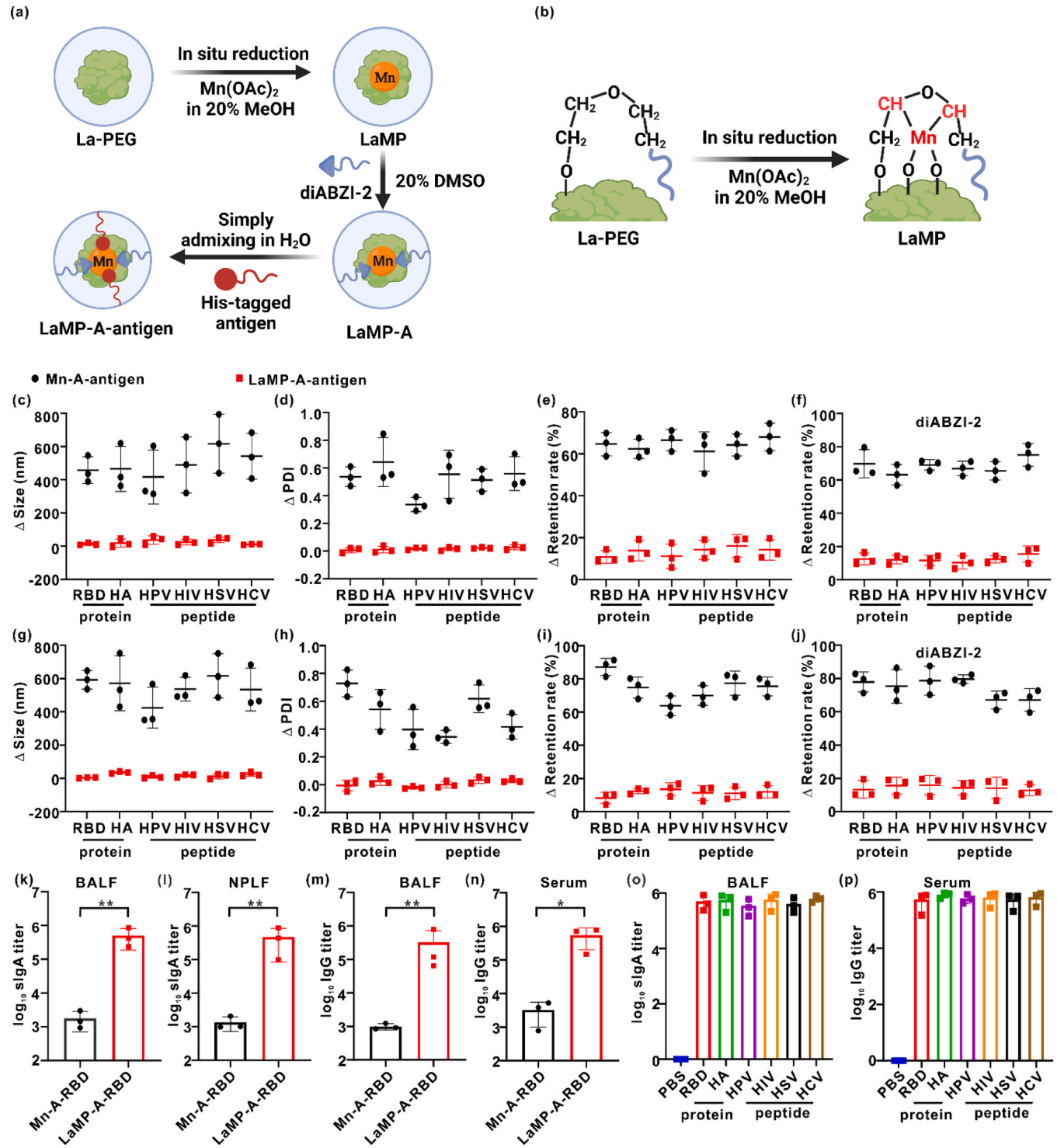


**Fig. 1.** His-tagged viral antigens bind to the LaMP metalloprotein. a, Schematic illustration of preparation of LaMP-A-antigen via in-situ reduction of Mn in protein–polymer conjugates. b, The mechanism of LaMP formation. c-f, Changes in size (c), PDI (d), antigen retention rate (e) and adjuvant diABZI-2 retention (f) of Mn-A-antigen and LaMP-A-antigen nanoparticles before and after lyophilization. g-j, Changes in size (g), PDI (h), antigen retention rate (i) and adjuvant diABZI-2 retention (j) of Mn-A-antigen and LaMP-A-antigen nanoparticles before and after incubation with 20% FBS for 24 h. k-n, RBD-specific sIgA antibody titers from BALF (k) and NPLF(l) and RBD-specific IgG antibody titers from BALF (m) and serum (n) detected by ELISA after intranasal administration of one single dose of Mn-A-RBD and LaMP-A-RBD nanoparticles in BALB/c mice, n 3. o,p, Different antigen-specific sIgA antibody titers from BALF (o) and different antigen-specific IgG antibody titers from serum (p) detected by ELISA after one single intranasal administration of LaMP-A-antigen nanoparticles (RBD, HA, antigen peptides of HIV, HPV, HCV, HSV) in BALB/c mice, n = 3.

γ and IL-12p70) [34]. We assumed that metal ions also played an important role in immune modulation for virus vaccination as well. Therefore, we screened various nutritive metal ions (such as $Ca^{2+}$, $Mg^{2+}$, $Mn^{2+}$, $Zn^{2+}$, $Cu^{2+}$, $Fe^{2+}$, $Fe^{3+}$, $Ni^{2+}$, $K^{+}$, and $Co^{2+}$) for immunity enhancement against SARS-CoV-2 pseudoviruses (SC2-PV, expressing SARS-CoV-2 S protein and GFP). A549 cells that can overexpress human ACE2 (A549/hACE2) were made first as an in vitro model, which were pre-incubated with different concentrations of metal ions for 24 h, and then SC2-PV (MOI = 0.1) was added. We found that the preincubation of $Mn^{2+}$ or $Co^{2+}$ induced less SC2-PV infection in a dose-dependent manner after challenge with GFP-labelled SC2-PV, indicated by the fluorescence intensity of GFP in the cells whereas other metals had negligible effect of immune modulation (Fig. S38a). This should be attributed to the activation of STING pathway and it has been previously reported that STING agonist pretreatment inhibited SARS-CoV-2 gene expression and replication in infected cells [46,47]. As shown in Fig. S38a,b, the immunity against SC2-PV (MOI = 0.1) was dose-dependent on the concentration of metal ions and diABZI-2, achieving a 39-fold dose saving effect. And the immunity was still pronounced even when SC2-PV reached MOI = 0.3 (Fig. S38c,d) and 0.6 (Fig. S38e,f), achieving a dose-saving effect of 21 and 2.6 times, respectively. Meanwhile, RBD has proven to be a viable immunogen for SARS-CoV-2 vaccine development, capable of triggering antigen-specific immune responses.[48] As shown in Fig. S38g, the addition of antigen RBD also enhanced the prophylactic effect. Since $Mn^{2+}$ has most pronounced synergy effect and has been approved by the US FDA for pharmaceutical use, [49] our following studies focused on the combination of $Mn^{2+}$, STING agonist and antigen RBD. In addition, similar levels of SC2-PV growth were observed when $Mn^{2+}$+diABZI-2 +RBD was added to A549/hACE2 cells 4 h before infection (T = −4 h) or 4 h after infection (T = 4 h) (Fig. S38h), suggesting that $Mn^{2+}$+diABZI-2 +RBD could be used as either vaccine or antivirus vector. In this study, we put the emphasis on the former.

Next, in order to verify the above phenomenon is caused by STING activation, IFN β in A549/hACE cells as an indicator of cGAS-STING pathway activation was measured [50]. Compared with other controls, A549/hACE cells treated with $Mn^{2+}$+diABZI-2 +RBD secreted more IFN β to form IFN β enhanceosome (Fig. S38i). Maximal transcription of the IFN-I gene was dependent on the formation of the enhanceosome containing phosphorylated IRF3 and p65 [51,52]. Activated IRF3 could translocate into the nucleus to induce the transcription of type I interferons and other inflammatory cytokines, resulting in an prophylactic effect [53]. Therefore, the effect of $Mn^{2+}$+diABZI-2 +RBD on the downstream of the STING-IFN-I signaling pathway was investigated. As shown in Fig. S38j, the combination of $Mn^{2+}$+diABZI-2 +RBD effectively enhanced the phosphorylation levels of TBK1, IRF3 and p65

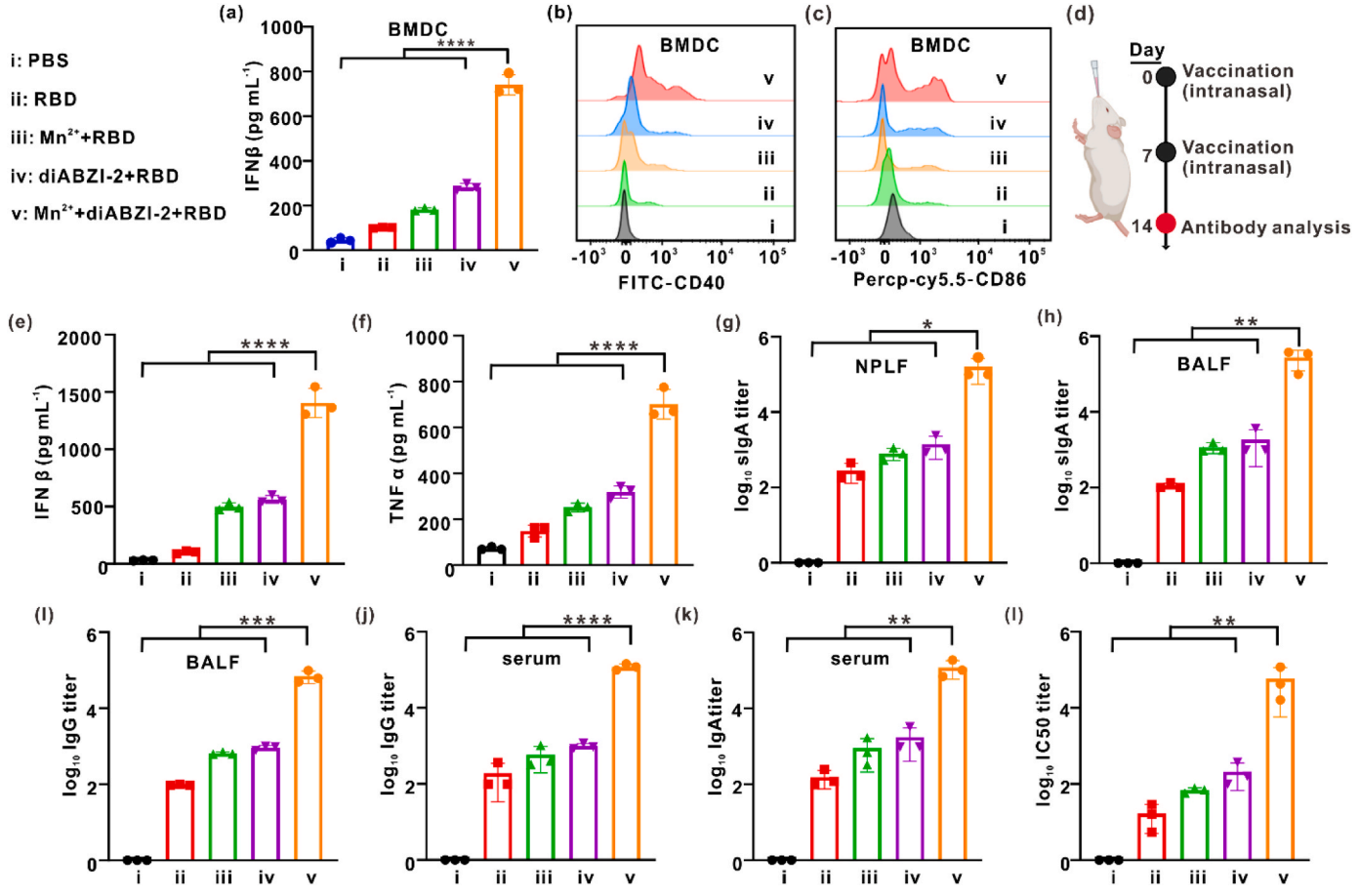


**Fig. 2.** $Mn^{2+}$ augments the activity of STING agonist diABZI-2. i: PBS, ii: RBD, iii: $Mn^{2+}$+RBD, iv: diABZI-2 +RBD, v- $Mn^{2+}$+diABZI-2 +RBD. a, BMDCs were treated with various samples as indicated with 200 μM $Mn^{2+}$, 1 μM diABZI-2 and 1 μg $mL^{-1}$ RBD for 24 h and then mouse IFN β secretion was quantified by ELISA. b,c, Representative flow cytometry plots of CD40 (b) and CD86 (c) in BMDCs treated with formulation i-v containing 200 μM $Mn^{2+}$, 1 μM diABZI-2 and 1 μg $mL^{-1}$ RBD for 24 h. d, Schematic illustration of animal study design. e,f, IFN β (e) and TNF α (f) from BALF detected by ELISA, n = 3. g,h, RBD-specific sIgA antibody titers from NPLF (g) and BALF (h) detected by ELISA, n = 3. i,j, RBD-specific IgG antibody titers from BALF (i) and serum (j) detected by ELISA, n = 3. k, RBD-specific IgA antibody titers from serum detected by ELISA, n = 3. l, Neutralization of pseudovirus.

in A549/ACE cells.

In addition, we also evaluated the effect of the combination of $Mn^{2+}$+diABZI-2 +RBD on immune cells such as bone marrow-derived dendritic cells (BMDCs) and bone marrow-derived macrophages (BMDMs). Similar to A549/ACE cells, $Mn^{2+}$ was able to enhance the STING agonist diABZI-2 activity and IFN-I secretion in BMDCs and BMDMs, producing IFN β enhanceosome (Fig. 2a-c and Fig. S38k,l). The combination of $Mn^{2+}$diABZI-2 +RBD also significantly upregulated CD40 and CD86 expression on BMDCs and CD86 expression on BMDMs (Fig. S38m).

We further assessed the in vivo immune responses against SARS-CoV-2 induced by Mn and diABZI-2, so BALB/c mice were intranasally administered with PBS, RBD, $Mn^{2+}$+RBD, diABZI-2 +RBD, $Mn^{2+}$+diABZI-2 +RBD (containing 15 μg $Mn^{2+}$, 5 μg diABZI-2 and 300 ng RBD) on days 0 and 7, and immunoassays were performed on day 14 (Fig. 2d). Compared with other controls, the combination of $Mn^{2+}$+diABZI-2 +RBD effectively activated the cGAS-STING pathway of cells in BALF, producing a large amount of IFN β (Fig. 2e)[46,54], TNF α (Fig. 2f) and chemokine CXCL 10 (Fig. S38n) that recruits adoptively transferred $CXCR3^+$ effector $CD8^+$ T cells.[55] To further assess mucosal immune antibody responses, we measured RBD-specific sIgA antibodies in NPLF and BALF of mice. Intranasal administration of $Mn^{2+}$+diABZI-2 +RBD produced the highest amount of RBD-specific sIgA antibodies in NPLF (Fig. 2g) and BALF (Fig. 2h). Antigen-specific sIgA responses provide a dynamic immune barrier preventing pathogen invasion.[56] Interestingly, RBD-specific IgG responses were also observed in BALF (Fig. 2i). Furthermore, inhalation of $Mn^{2+}$+diABZI-2 +RBD induced the most RBD-specific IgG antibodies (Fig. 2j) and RBD-specific immunoglobulin A (IgA) antibodies in serum (Fig. 2k). And the antibodies produced in serum could neutralize the SARS-CoV-2 virus (Fig. 2l and Fig. S38o). These results suggested $Mn^{2+}$+diABZI-2 +RBD could effectively stimulate strong metalloimmune responses in forms of mucosal and humoral immunity against SARS-CoV-2.

*Preparation and characterization of lyophilizable LaMP-A-RBD*

Although Mn+A+RBD induced promising immune responses, the Mn+A+RBD mixture had disadvantages such as low limited endocytosis and rapid clearance rate. Therefore, STING agonist, and antigen RBD were chelated on LaMP and the image of SDS-PAGE gel verified the

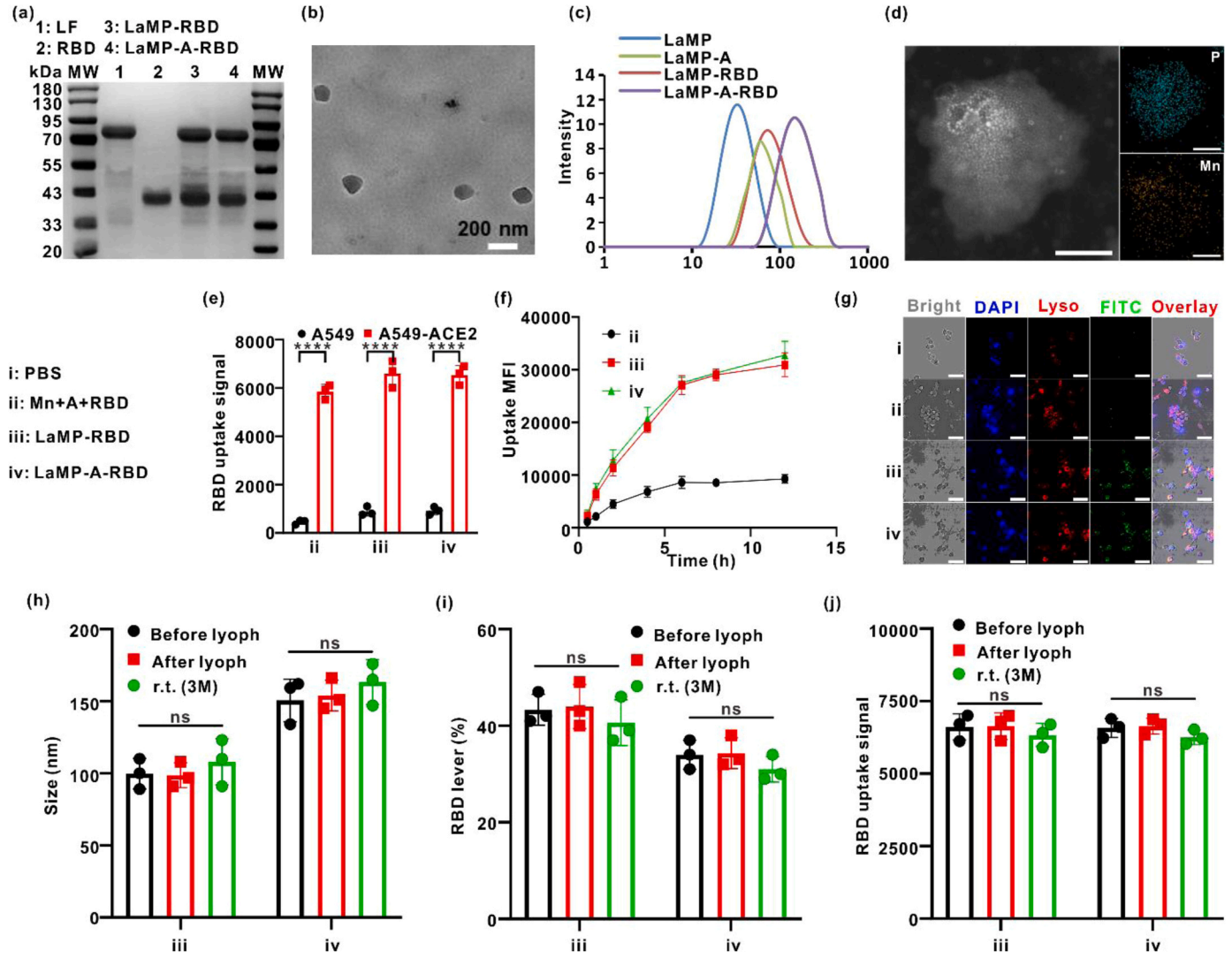


**Fig. 3.** Preparation and characterization of lyophilizable LaMP-A-RBD a, SDS–PAGE gel of different samples as indicated. b, TEM image of LaMP-A-RBD. c, Dynamic light scattering of different sample. i: PBS, ii: Mn+A+RBD, iii: LaMP-RBD, iv: LaMP-A-RBD. d, STEM image of LaMP-A-RBD and the corresponding elemental mapping for P and Mn. Scale bars: 200 nm. e, Binding of FITC-labeled RBD, in soluble or particulate form, to hACE2-expressing cells. f,g, Cellular uptake of difference formulations. BMDCs were incubated with Mn+A+RBD (FITC-RBD, diABZI-2 and Mn), LaMP-RBD (FITC) and LaMP-A-RBD (FITC) for different times, followed by analysis of intracellular fluorescence of FITC by microplate reader (f) and confocal microscopy (g), Scale bars, 50 μm. h–j, Size change (h), RBD level change (i) and binding of FITC-labeled RBD (j) of LaMP-RBD or LaMP-A-RBD after lyophilization.

successful conjugation on LaMP (Fig. 3a). The LaMP-A-RBD exhibited spherical morphology as shown in Fig. 3b. The hydrodynamic diameter of LaMP-A-RBD was 130 ± 21 nm with a polydispersity index (PDI) of 0.154, measured by dynamic light scattering in Fig. 3c. The corresponding energy dispersive X-ray spectra and Mn2p X-ray photoelectron spectroscopy spectra further confirmed the successful confinement of Mn in LaMP (Fig. 3d and Fig. S39). $Mn^{2+}$, diABZI-2 and RBD were more easily released from LaMP-A-RBD at pH= 5.5, likely because the ester bond between PEG and LF was cleaved at pH= 5.5 (Fig. S40).

To study the cellular uptake by A549/hACE2, RBD protein was fluorescently labelled by Fluorescein 5-isthiocyanate (FITC). As shown in Fig. 3e, significant uptake was observed when A549/hACE2 was incubated with Mn+A+RBD, LaMP-RBD or LaMP-A-RBD, whereas the same cell line lacking hACE2 expression (A549) exhibited minimal cellular uptake of RBD. It showed that after chelation, RBD remained its capability of combining with hACE2 of SARS-CoV-2. We further investigated the uptake of LaMP-A-RBD by immune cells BMDC in vitro. Mn+A+RBD form was poorly internalized by BMDC, while LaMP-A-RBD and LaMP-RBD with RBD labelled by FITC showed significantly increased cellular uptake (Fig. 3f and Fig. S41). Confocal microscopic images also showed that LaMP-A-RBD and LaMP-RBD were up taken more than controls and they were able to escape from lysosomes, delivering Mn, diABZI-2 and RBD to the cytoplasm for cGAS-STING pathway activation (Fig. 3g). Compared with the Mn+A+RBD, LaMP-RBD and LaMP-A-RBD vaccines were more efficacious to prevent SC2-PV infection by enhancing adaptive immunity, but the prophylactic rate of LaMP-RBD was significantly lower than that of LaMP-A-RBD (Fig. S41c). Since it was desired to transport and store clinical freeze-dried vaccine as solid powder, LaMP-based formulations were lyophilized and stored at room temperature for 3 months. After hydration, the size, RBD content and cellular uptake by A549/hACE2 cells of LaMP-A-RBD before and right after or 3 months after lyophilization and storage were compared

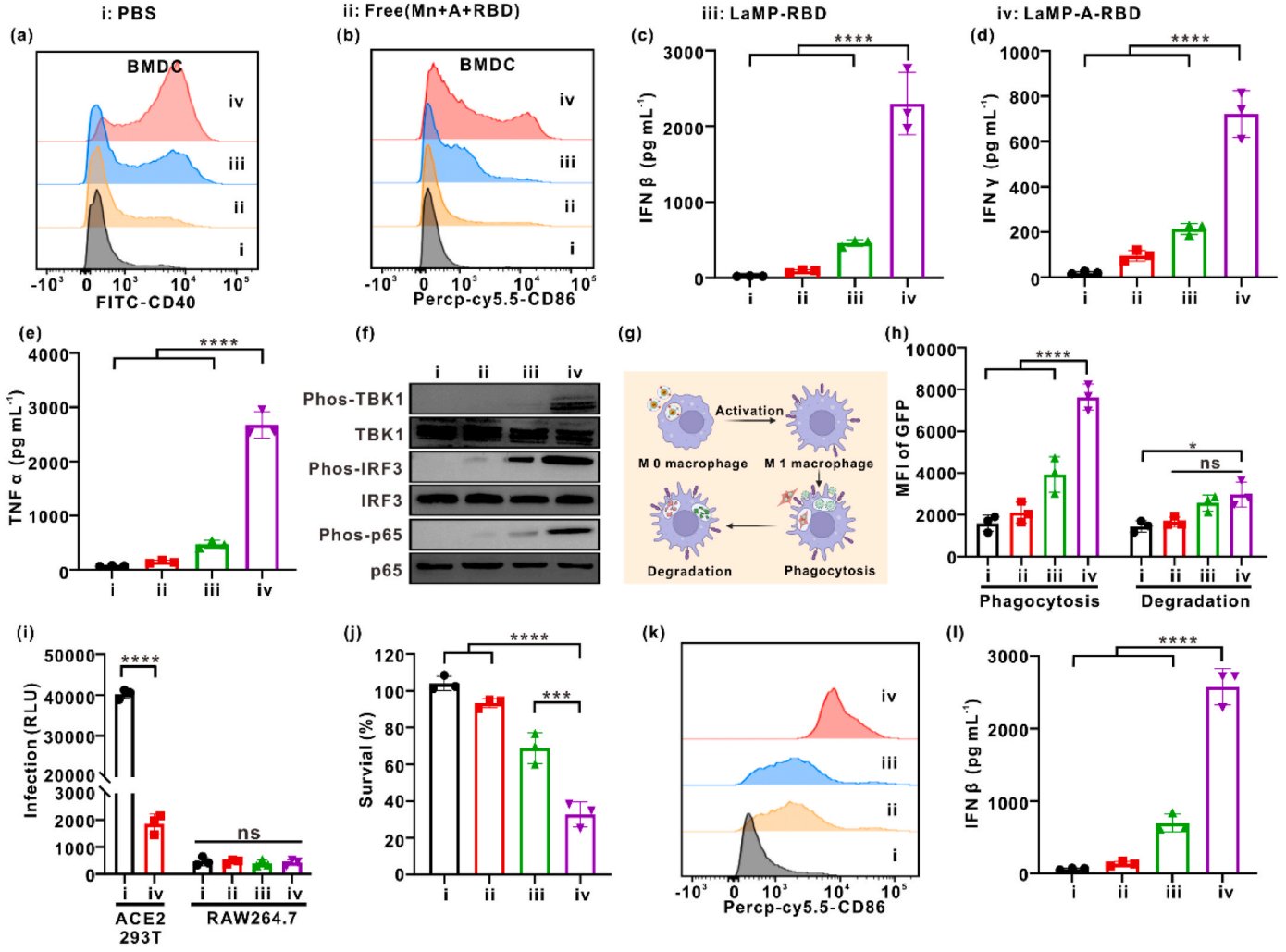


**Fig. 4.** LaMP-A-RBD activates immune cells to induce the phagocytosis. i: PBS, ii: Mn+A+RBD, iii: LaMP-RBD, iv: LaMP-A-RBD. a,b, BMDCs were treated for 24 h with formulation i-iv, followed by the analysis for CD40 (a) and CD86 (b) expression by flow cytometry. c-e, BMDCs were treated with formulation i-iv containing 500 ng $mL^{-1}$ RBD, 500 ng $mL^{-1}$ diABZI-2 and 12 μM $Mn^{2+}$ for 24 h, and then IFN β (c), IFN γ (d) and TNF α (e) secretion was quantified by ELISA. f, Western blot analysis of the activation of the cGAS-STING-IFN-I pathway in BMDCs after treatment with formulation i-iv containing 500 ng $mL^{-1}$ RBD, 500 ng $mL^{-1}$ diABZI-2 and 12 μM $Mn^{2+}$ for 6 h, representative data from two independent experiments with similar results are shown. TBK1, IRF3, and p65 were used as the loading controls. g, Illustration of phagocytosis and elimination of SARS-CoV-2 induced by LaMP-A-RBD via activating the macrophages. h, Quantitative analysis of phagocytosis and elimination of SC2-PV (expressing GFP) in RAW264.7 macrophages (M 0) primed by the formulation i-iv containing 500 ng $mL^{-1}$ RBD, 500 ng $mL^{-1}$ diABZI-2 and 12 μM $Mn^{2+}$. i, Macrophages were pretreated with formulation i-iv for 4 h, and infected with the indicated GFP-tagged SARS-Cov-2 0.1 MOI for 48 h, SARS-Cov-2 GFP expression was determined. j, Macrophages pretreated with preparations i-iv were incubated with ACE2/HEK293 cells pre-infected with SARS-Cov-2 pseudovirus for 48 h, and the activity of ACE2/HEK293 cells was analyzed by CCK8 kit. **k,** CD86 expression in RAW264.7 macrophages (M 0) after incubation with formulation i-iv for 48 h. **l,** RAW264.7 macrophages (M 0) were treated with formulation i-iv with 500 ng $mL^{-1}$ RBD, 500 ng $mL^{-1}$ diABZI-2 and 12 μM $Mn^{2+}$ for 24 h, and then IFN β secretion was quantified by ELISA.

(Fig. 3h-j), showing that freeze-drying and storage at room temperature did not affect the size and binding capacity of RBD to hACE2. In addition, diABZI-2 and RBD of LaMP-A-RBD retention rate still reached > 95% in serum up to 5 days (Fig. S42).

*LaMP-A-RBD activates DC and macrophages*

DC maturation and macrophage activation play a key role in activating immune responses.[57] The LaMP-A-RBD induced DC maturation **(Fig. 4a,b)** and IFN β response (Fig. 4c) more significantly than other controls. Similarly, type II interferons (such as IFN γ) and TNF α were also induced (Fig. 4d,e), because LaMP-A-RBD could promote the phosphorylation of TBK1, and IRF3 proteins and activate the cGAS-STING pathway in BMDCs (Fig. 4f). Type I interferons induced the expression of various interferon-stimulated genes that interfere with viral replication. SC2-PV were effectively phagocytized by macrophage RAW264.7 treated by LaMP-A-RBD for 24 h, and the virus was effectively neutralized in the subsequent degradation process, but Mn+A+RBD and LaMP-RBD induced weaker SC2-PV phagocytosis and degradation in macrophage RAW264.7 (Fig. 4g). Presumably, LaMP-A-RBD polarized macrophage from M 0 to M 1, leading to enhanced phagocytosis, which was important for viral infection prevention, phagocytosis and elimination (Fig. 4h).[57] Uptake of SC2-PV did not cause infection of macrophages, because no significant virus release was observed in culture (Fig. 4i). Besides, CCK8 assay showed that LaMP-A-RBD induced macrophages activation to kill A549/hACE cells infected with SC2-PV by phagocytosis (Fig. 4j). This may be because LaMP-A-RBD-mediated co-delivery of $Mn^{2+}$, diABZI-2 and RBD to RAW264.7 activated macrophages (Fig. 4k), and promoted the secretion of cytokines IFN β and TNF α (Fig. 4l and Fig. S43).

*LaMP-A-RBD vaccination induces mucosal immune response in a hamster infection model*

We next explored whether LaMP-A-RBD can in vivo promote and amplify mucosal, cellular and humoral immunity to prevent SARS-CoV-2 infection after vaccination (Fig. S44). Given that SARS-CoV-2 was unable to bind to murine ACE2, we selected 5–6-week-old female hamsters for animal model establishment. Since the mucosa is the main route of entry for pathogens, activation of the mucosal immune response could be a solution for neutralizing pathogen[58]. Hamsters were inhaled various formulations including PBS, Mn+A+RBD and LaMP-RBD and experimental group of LaMP-A-RBD (containing 50 μg $Mn^{2+}$, 30 μg diABZI-2 and 500 ng RBD). 2 weeks after vaccination,

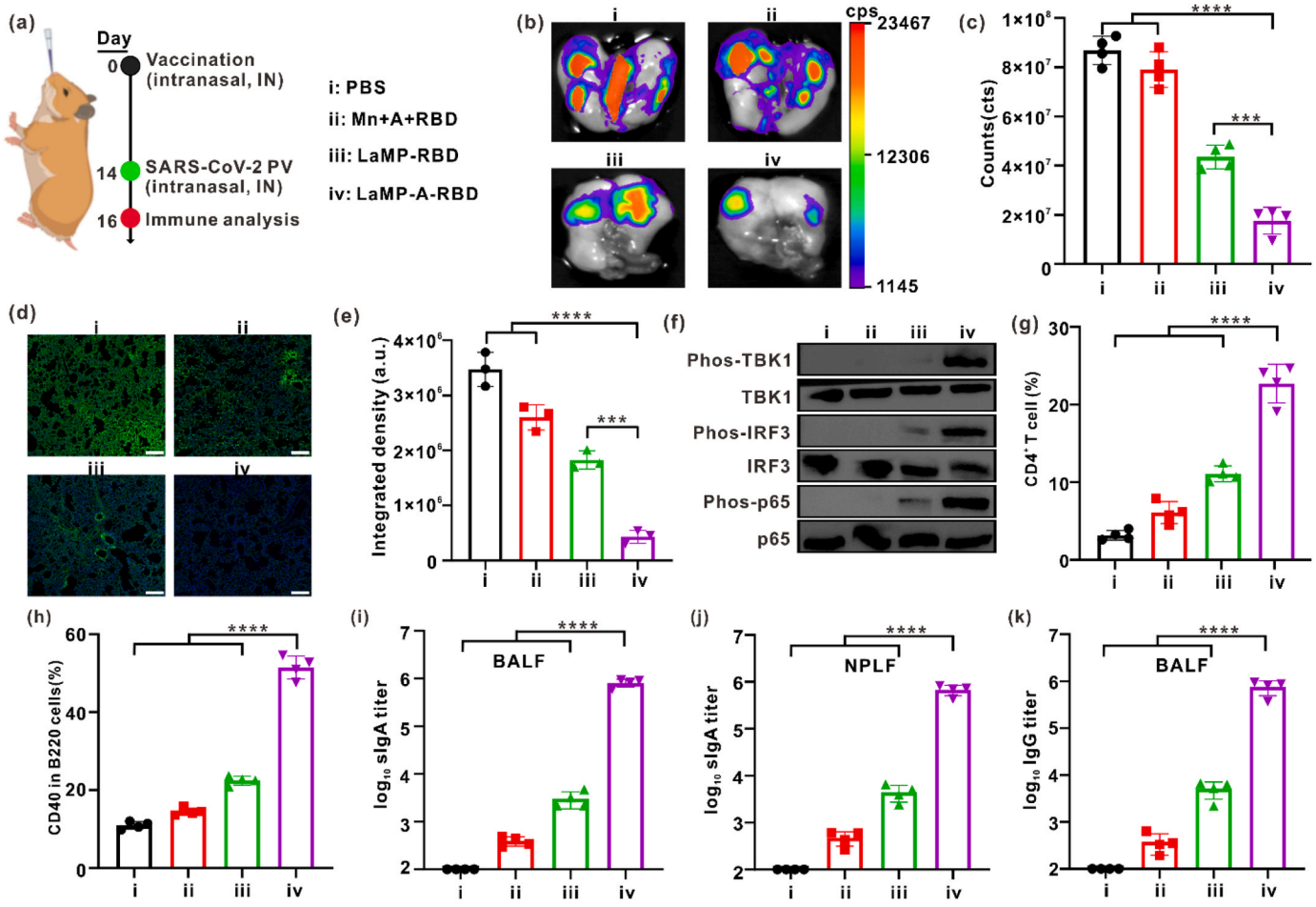


**Fig. 5.** Vaccination of hamsters with LaMP-A-RBD induces mucosal immunity efficiently neutralizing SARS-CoV-2 pseudovirus. a, Schematic illustration of LaMP-A-RBD vaccination in hamster. i: PBS, ii: Mn+A+RBD, iii: LaMP-RBD, iv: LaMP-A-RBD. b, c, Ex vivo imaging of lungs (b) and quantification (c) of GFP fluorescence in lungs for vaccinated mice that were inoculated with SARS-CoV-2 pseudovirus with GFP expression., n = 4 per group. d, Immunostaining imaging of parenchyma of hamsters with different vaccinations. Nuclei stained by DAPI shown was in blue and SARS-CoV-2 pseudovirus expressing GFP was shown in green. e, Quantification of SARS-CoV-2 pseudovirus with GFP fluorescence from parenchyma. f, Western blotting analysis of TBK1, IRF3, p65 and phosphorylation of the proteins in pneumocytes. g, Quantification of $CD4^+CD3^+$ T cells in BALF derived from vaccinated hamsters. h, Quantification of B cell activation in BALF derived from vaccinated hamsters. i,j, RBD-specific sIgA antibody titers from BALF (i) and NPLF (j) measured by ELISA, n = 4.k, RBD-specific IgG antibody titers in BALF of hamsters detected by ELISA.

hamsters were intratracheally challenged by SC2-PV (Fig. 5a). Subsequently, lung tissues were imaged to evaluate the neutralize SC2-PV after hamsters was sacrificed and challenged. The GFP signal in LaMP-A-RBD group was significantly reduced, indicative of effective neutralize SC2-PV (Fig. 5b,c). Immunostaining imaging of the parenchyma demonstrated that less SC2-PV was distributed in parenchyma with vaccination by LaMP-A-RBD than that in the Mn+A+RBD and LaMP-RBD group (Fig. 5d,e).

To further investigate the mechanism of mucosal immune response by LaMP-A-RBD, we collected NPLF and BALF for immunoassay. First, similarly as the in vitro results discussed above, hamsters with inhalation of LaMP-A-RBD significantly activated cGAS-STING pathway in NPLF and BALF cells and induced TBK1, p65 and IRF3 phosphorylation (Fig. 5f). The IFN β secretion in the LaMP-A-RBD group was about 9-fold and 4-fold higher than that in Mn+A+RBD and LaMP-RBD groups, respectively (Fig. S45a). This may be because the $Mn^{2+}$+ diABZI-2 +RBD mixture could not be effectively taken up by cells. The increased secretion of IFN β and the chemokine CXCL10 further supported that LaMP-A-RBD induced activation of the STING pathway (Fig. S45b). Also, LaMP-A-RBD synergistically amplified the activation of STING agonist diABZI-2. It was also previously demonstrated that type I interferons play an important role in preventing severe COVID-19 and protect the body against viral infection[59]. We assumed that IFN β secretion via STING pathway activated by LaMP-A-RBD further promoted DC maturation. Subsequently mature DCs secreted a variety of pro-inflammatory cytokines to regulate differentiation and recruitment of T cells. To test this hypothesis, we measured mature DC in the lavage fluid by flow cytometry analysis. The $CD40^+CD86^+$ DC of LaMP-A-RBD was nearly 3-fold and 2-fold higher than that of Mn+A+RBD and LaMP-RBD, respectively (Fig. S46). The secretion levels of pro-inflammatory cytokines interleukin 12p70 (IL-12p70) and TNF α were also enhanced (Fig. S47a,b). Presumably, antiviral cytokines (such as TNF α, IL-12p70) are produced early after infection and the inflammatory chemokines might play an important role in innate antiviral defense by coordinating the responses of macrophages, neutrophils, DC cells, and NK cells at the site of infection. However, in a later phase after infection, viral infection should be promptly neutralized by antibodies and immune cells, resulting in reduced inflammatory responses. Therefore, more future work is needed to assess toxicity of the vaccine in hamsters and other species.

Although T cells and B cells do not directly confer sterilizing immunity, they are involved in limiting viral spread and preventing aggravation after the virus is first neutralized by humoral immunity, and $CD4^+$ T cells that participate in antigen recognition by TCR of helper T cells.[60] As shown in Fig. 5g and Fig. S47c, LaMP-A-RBD increased $CD4^+$ T cells in the BALF, demonstrating that antigen presentation further aided B cell activation. B lymphocytes are transformed into plasma cells under the stimulation of antigens, and produce antibodies specifically binding to antigens to neutralize the invading virus.[60] After B cells are activated, CD40 markers are expressed on the surface. Thus, we measured the level of CD40 on the surface of B cells in BALF by flow cytometry (Fig. 5h and Fig. S48). Compared with Mn+A+RBD and LaMP-RBD, inhalation of LaMP-A-RBD induced a higher expression level of CD40 on the surface of B cells. In addition, inhalation of LaMP-A-RBD produced the highest amount of sIgA antibodies in BALF (Fig. 5i) and NPLF (Fig. 5j). Interestingly, a detectable IgG response against RBD was also observed in BALF (Fig. 5k). These results indicated that the LaMP-A-RBD vaccination could effectively generate large amounts of sIgA neutralizing pathogens by amplify STING activation and IFN-I secretion to stimulate the respiratory mucosal immune system.

*Cellular response by LaMP-A-RBD vaccination*

Since spleen is an important immune organ, we further evaluated whether the inhalable LaMP-A-RBD metal-based vaccine could effectively activate the metalloimmune response in spleens. After vaccination of hamsters by the formulations as indicated, spleens were removed for immunoassay. It was found that the spleens in the LaMP-A-RBD vaccination group was significantly heavier than that in other control groups (Fig. S49a,b). We supposed that it should be some immune responses caused by either virus or vaccines or both that induced splenomegaly, which needs further investigation. We also detected the activation of cGAS-STING pathway in splenocytes. Similarly, LaMP-A-RBD also effectively induced STING-dependent phosphorylation of TBK1, p65 and IRF3 in splenocytes too (Fig. S49c). Activated IRF3 could translocate into the nucleus to induce the transcription of type I interferons and other inflammatory cytokines to establish a protective immunity state.[53] LaMP-A-RBD induced effective secretion of cytokines including IFN β, CXCL 10, IL-12p70 and TNF α in splenocytes of hamsters inhaling LaMP-A-RBD (Fig. 6a-c and Fig. S49d). Among them, the secretion of IFN β in the LaMP-A-RBD group was nearly 14 times and 5 times than that of the Mn+A+RBD and the LaMP-RBD groups, respectively (Fig. 6a). IFN β can induce a large number of downstream IFN-stimulated genes (ISGs) to establish a "protective immunity state" in host cells to prevent viral infection.[61] And pro-inflammatory cytokines and chemokines enhance the adaptive immune response and recruit a variety of immune cells to further prevent viral infection and restrain viral spread.[62] In addition, splenocytes were analyzed by enzyme-linked immunosorbent spot (ELISpots) for IFN γ. LaMP-A-RBD induced significantly higher IFN γ secretion (Fig. 6d). Specifically, LaMP-A-RBD inhalation induced approximately 500 spot-forming units (s.f.u.) per $10^6$ splenocytes, significantly higher than other control groups (Fig. 6d). Since presentation of viral antigens to antigen-presenting cells (APCs) such as DCs is also important for protection against pathogens,[63] splenocytes after one single immunization was collected and restimulated with RBD to assess DC activation by flow cytometry. In splenocytes, more DCs were activated with greater proportion of $CD40^+CD86^+$ after hamsters were vaccinated by LaMP-A-RBD (Fig. 6e,f). In addition, macrophage activation can not only facilitate phagocytosis and elimination of viruses, but also enhance the antigen presentation of MHC II molecules on macrophages, resulting in adaptive immune responses.[57] Therefore, we studied the expression of $CD86^+$ on F4/80 macrophages. In splenocytes from the LaMP-A-RBD group, a greater proportion of F4/80 was $CD86^+$, indicating that more macrophages were efficiently activated (Fig. 6g,h). Moreover, natural killer cells (NK) play an important role in innate immunity to protect against viral infection, not only by directly targeting and killing infected cells, but also by regulating adaptive T-cell responses.[64,65] Thus, we also detected the NK cell activity in splenocytes and found that compared with the Mn+A+RBD and LaMP-RBD groups, the proportion of NK cell activity in splenocytes vaccination by LaMP-A-RBD increased by nearly 5 times and 3 times (Fig. 6i,j), because $Mn^{2+}$ enhanced diABZI-2 activity and amplified IFN-I response, resulting in generation of more IFN β and IL-12p70 cytokines (Fig. 6a, c). IFN β and IL-12p70 cytokines were shown to increase NK cell cytotoxicity, but also protect NK cells from "cannibalism", thereby promoting population expansion and preventing infection.[66,67].

*T cell response of LaMP-A-RBD vaccination after virus challenge*

$CD4^+$ T cells are critical for long-term immunity and memory by T helper 1 (TH1) and T follicular helper (TfH) cells. The adaptive immune system provides robust and durable cellular and humoral immunity, coupled with T-cell and B-cell responses to fight against SARS-CoV-2.[60] We therefore examined systemic T and B cell responses following vaccinations by inhalable LaMP-A-RBD. Notably, inhalation of LaMP-A-RBD resulted in higher frequency of $CD4^+$ T cells (Fig. 7a and Fig. S50a) and RBD-specific activated B cells (Fig. 7b,c). Next, we collected spleens to study the induction of memory T cell responses and found that the number of effector memory T cells ($T_{EM}$, $CD44^+CD62L^-$) and central memory T cells ($T_{CM}$, $CD44^+CD62L^+$) only increased slightly after vaccination by Mn+A+RBD and LaMP-RBD, indicating that

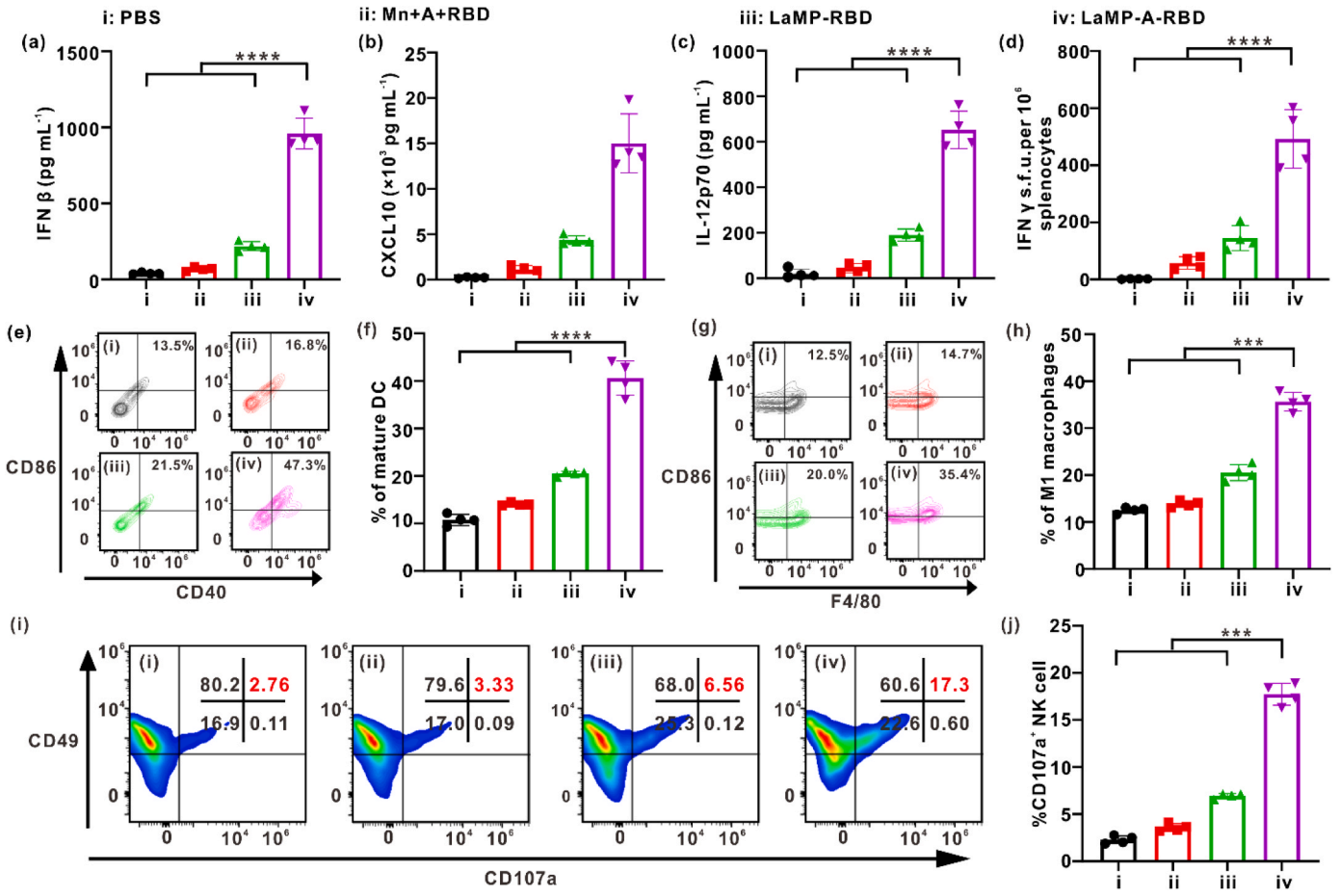


**Fig. 6.** Vaccination of hamsters with LaMP-A-RBD elicited immunity against virus via regulating cellular response. a-c, IFN β(a), CXCL-10(b) and IL-12p70(c) levels from splenocytes supernatant restimulated by RBD, n = 4. d, Number of IFN γ spots in a 96-well plate with $10^6$ splenocytes per well after rechallenge with RBD. Splenocytes were derived from each group intranasally given formulation i-iv, IFN γ splenocytes shown as s.f.u. per $10^6$ cells, n = 4. e, Flow cytometry analysis of DC maturation (gated on $CD11c^+$ DCs) in the splenocytes derived from vaccinated hamsters. f, Quantification of DC maturation (gated on $CD11c^+$ DCs) in the splenocytes derived from vaccinated hamsters. g, Representative flow cytometry analysis images of $F4/80^+CD86^+$ cells in splenocytes. h, Relative quantification of $F4/80^+CD86^+$ cells in the splenocytes. i, Representative flow cytometry analysis images and j, Relative quantification of $CD49^+CD107a^+$ cells in splenocytes of vaccinated hamsters. i: PBS, ii: Mn+A+RBD, iii: LaMP-RBD, iv: LaMP-A-RBD.

Mn+A+RBD were rapidly metabolized and pure manganese had little effect on $T_{EM}$ and $T_{CM}$ activation. In contrast, inhaled LaMP-A-RBD stimulated higher levels of memory T cells (Fig. 7d,e), showing its great potential of induction of strong immune memory. $T_{EM}$ immediately initiate an immune response by secreting effector molecules after stimulation by antigens once virus evades[68] As shown in Fig. 7f, inhalation of LaMP-A-RBD generated the most specific anti-RBD antibody in mouse serum. In particular, the IgG subclass was further assessed and LaMP-A-RBD effectively elicited most type 1 T helper (Th1) immune response among these groups with an IgG2a/IgG1 ratio more than 1 (Fig. 7g). In addition to IgG isotypes, LaMP-A-RBD also substantially produced more RBD-specific IgA antibodies in serum than other groups (Fig. 7h). Moreover, the SC2-PV neutralization capability of antibodies produced in serum was evaluated. Neither the IgA nor IgG antibodies of the hamster vaccinated by PBS could prevent the entry of the SC2-PV into A549 cells expressing the ACE2 receptor. Compared with the Mn+A+RBD and LaMP-RBD groups, serum obtained from hamsters immunized by LaMP-A-RBD had significant SC2-PV neutralizing activity owing to the synergistically enhanced metalloimmune responses and cGAS-STING pathway activation induced by this new metal-based nanovaccine of LaMP-A-RBD (Fig. 7i and Fig. S50b). Also, Hematoxylin and eosin staining suggested that inhalation of LaMP-A-RBD did not cause overt acute toxicity (Fig. S51). These datasets demonstrated that LaMP-A-RBD inhalation had good biocompatibility and strongly induces systemic T-cell and B-cell immune responses by activating the cGAS-STING pathway in splenocytes to generate type I interferon enhancer.

*Immunity of LaMP-A-RBD vaccination with no virus challenge*

To further verify that the LaMP-A-RBD vaccine could also triggers mucosal, cellular and humoral immunity prior to viral challenge to rule out the interference of virus with the immunity evaluation, female BALB/c mice aged 6 to 8 weeks were immunized intranasally with LaMP-A-RBD vaccine on day 0 and boosted on the day 14. Lymph nodes, spleens and blood were collected for immune analysis on the day 17. Alum adjuvant that is a commercial adjuvant facilitating antigens promoting immune responses was used as a control (alum+RBD). As shown in Fig. S52 a-c, in lymph nodes, LaMP-A-RBD vaccine could promote dendritic cell maturation and activate downstream T cells ($CD4^+$ and $CD8^+$ T cells). Compared to Alum+RBD, LaMP-A-RBD vaccine was even better to activate T cells. Similarly, for DC, T cell, NK cell and B cell activation in spleen, LaMP-A-RBD vaccine also out-performed alum+RBD and other control groups (Fig. S52d-h). The activation of $CD4^+$ T cells and B cells was shown more conducive to the production of antigen-specific antibodies. Cytokines including IFN β, TNF α, IL-12p70

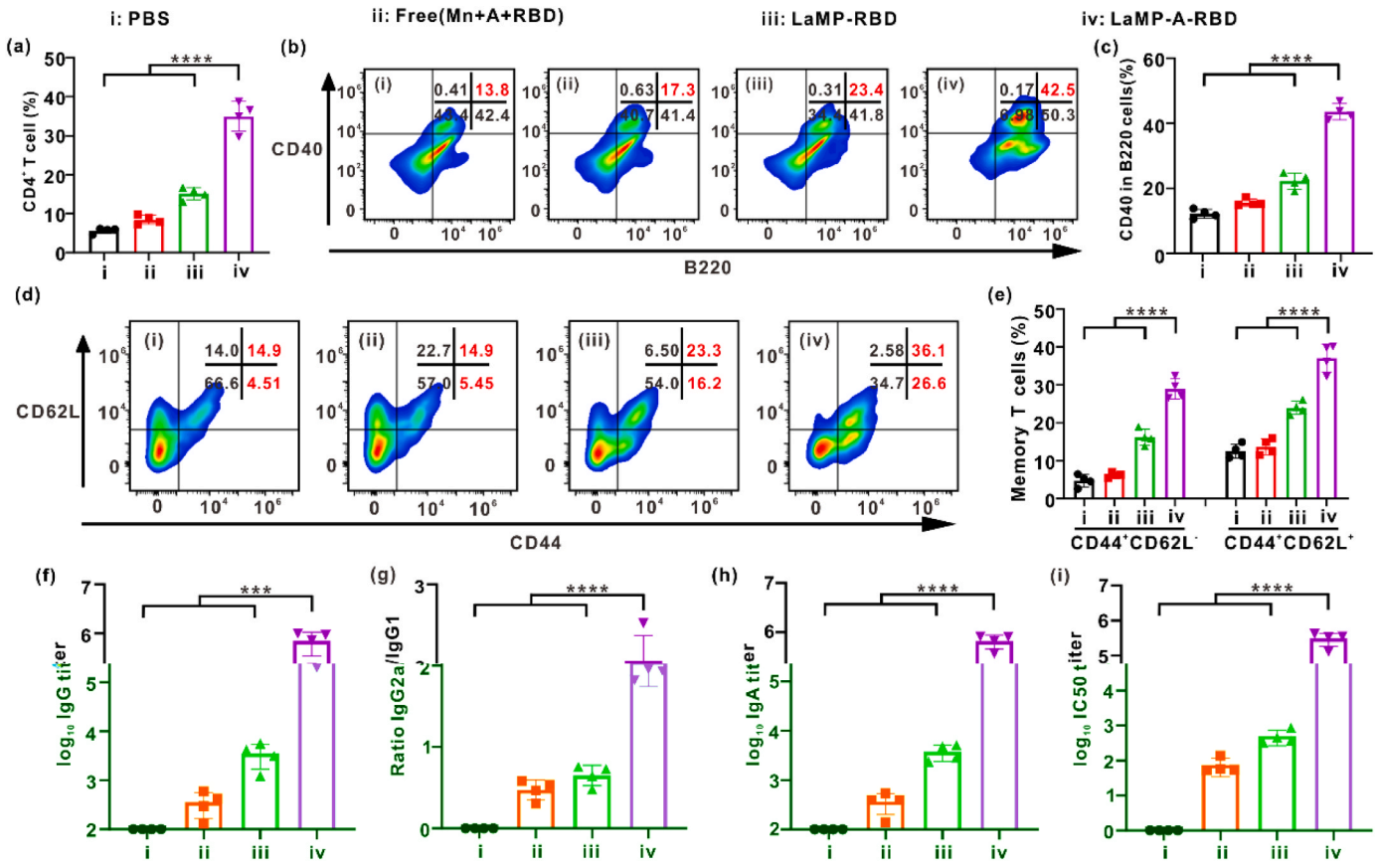


**Fig. 7.** Effective induction of T cell immune response after vaccination by LaMP-A-RBD. a, RBD-specific $CD4^+$ T cells in the splenocytes of hamsters collected one week after the last vaccination by different formulations as indicated, i: PBS; ii: Mn+A+RBD; iii: LaMP-RBD; iv: LaMP-A-RBD, n = 4. b,c, Representative flow cytometry plots (b) and quantification (c) of B cell activation in splenocytes collected from vaccinated hamsters. d,e, Representative flow cytometry plots (d) and quantification (e) of $T_{EM}$ ($CD44^+CD62L^-$) and $T_{CM}$ ($CD44^+CD62L^+$) in the splenocytes of vaccinated hamsters. f, Anti-RBD antibody titers from murine serum measured by ELISA, n = 4. g, Ratio of RBD-specific IgG2a to IgG1 antibody after vaccination on hamsters, n = 4. h, RBD-specific IgA antibody titers in serum of hamster after one dose of vaccination with LaMP-A-RBD and other controls as labelled. i, Antibody neutralization assay against SC2-PV using serum of hamsters.

were significantly boosted after immune cells were activated (Fig. S52i-k), demonstrating that the LaMP-A-RBD vaccine induced a strong cellular immune response in vivo. More importantly, LaMP-A-RBD activated a strong metal immune response in DCs after inhalation, producing a large amount of IFN β to activate other immune cells (Fig. S52i). Since the production of antibodies was particularly critical for viral vaccination. Next, we assessed antibody levels in BALF, NPLF, and serum. Compared with PBS, RBD and Mn+A+RBD, both LaMP-RBD and Alum+RBD induced more obvious sIgA and IgG antibody production, which made alum adjuvant widely used in vaccines. We also found LaMP-A-RBD vaccine outperformed Alum+RBD, inducing more sIgA and IgG antibody production and stronger mucosal and humoral immunity (Fig. S52l-m). Serum antibodies obtained from mice immunized with alum+RBD could effectively neutralize PsV, however, immunization with LaMP-A-RBD vaccine showed higher PsV neutralizing activity (Fig. S53o). These sets of data suggested that LaMP-A-RBD vaccine was more capable of inducing cellular, humoral and mucosal immune responses in vivo than commercial alum adjuvant, highlighting the great potential of LaMP-A-RBD vaccine in clinical applications.

*Memory and safety of LaMP-A-RBD vaccination*

To assess whether LaMP-A-RBD can induce immune memory after intranasal vaccination, we collected mouse spleens on the day 30 after intranasal vaccination to study the induction of memory T cell responses. Indeed, inhaled LaMP-A-RBD vaccine elicited higher levels of memory T cells ($T_{EM}$ and $T_{CM}$), confirming LaMP-A-RBD can induce great immune memory (Fig. S53). At last, we further investigated the safety of LaMP-A-RBD by measuring the body weight of the mice and blood analysis after mice were vaccinated. We found that the spleen did not become enlarged (Fig. S54a,**b**). Body weight did not change significantly during the experimental period (Fig. S54c). And the hematological parameters of mice immunized with LaMP-A-RBD twice had no significant difference from that of the PBS group (Fig. S54d). These results show that inhalation of LaMP-A-RBD vaccine did not cause overt toxicity.

## Conclusion

In summary, we have developed a generalized metal-based nanovaccine platform that remains stable in serum and can be lyophilized for long-term storage at room temperature for at least three months. Using the metal core of LaMP as a scaffold, adjuvants with imidazole group such as ABZI, CDA, diABZI-2 can be coordinated generating LaMP-A that can synergistically activate cGAS-STING pathway. Furthermore, versatile virus antigens (such as RBD, HA, antigen peptides of HIV, HPV, HCV, HSV and others) could be also coordinated by simple admixture in aqueous solution. LaMP-A-antigen allows immune cells for establishment of a protective immunity state for infection prevention, because $Mn^{2+}$ enhances the adjuvant activity of diABZI-2 and amplifies the IFN-I responses. After one single intranasal vaccination of LaMP-A-RBD in hamsters, strong mucosal, humoral and cellular immunity were induced

in vivo to protect lungs from virus infection into the airway mucosa. Antibodies in serum were also able to neutralize SARS-Cov-2 pseudovirus. This nanoplatform could be generalized to other vaccine manufacture for the management of a variety of infectious viral diseases. Future research directions include efficacy studies on real virus and more mechanism investigations for the use of this new metal-based vaccine.

## Materials and methods

### *Synthesis of diABZI-2*

See supplementary information.

### *Cell lines*

A549 cell (BNCC337696) were purchased from the Beijing BeNa Culture Collection. DC2.4 cells were purchased from ORiCells Biotechnology Co., Ltd (Shanghai). The cells were cultured in 1640 or DMEM medium with 100 U $mL^{-1}$ of streptomycin, 100 U $mL^{-1}$ of penicillin, and 10% FBS (Yeasen, Shanghai, China) at 37 °C in a humidified incubator with 5% $CO_2$.

### *Synthesis and characterization of LaMP-A-antigen*

For CHO-PEG2000 grafted lactoferrin (La), 29.43 mmol La and 0.125 mmol CHO-PEG2000 were dissolved in 20 mL distilled water, and 3 mg $mL^{-1}$ sodium cyanoborohydride was added to react for 20 h. In order to remove unreacted CHO-PEG2000, 3500 Da dialysis bag was used for dialysis for 24 h, and then subjected to freeze-dry to obtain La-PEG.

The obtained La-PEG and manganese acetate (m:m = 10:1) were added to a mixed solution of 20% methanol and 80% $H_2O$ and stirred for 20 h, and then dialyzed with 3500 Da dialysis bag for 24 h to remove excess manganese acetate. Finally, freeze-dry to obtain metal core (**La**-**Mn**-**P**EG, termed LaMP). In order to chelate diABZI-2 and antigen proteins or peptides, LaMP and diABZI-2 were added ($n_{Mn}$:$n_{diABZI\text{-}2}$ = 1:1) 20% DMSO aqueous solution was stirred for 10 h, and then directly lyophilized to remove DMSO. The LaMP-A reconstituted in water was centrifuged (2000 rcf, 5 min) to remove unchelated diABZI-2. Different antigen (RBD, Flu, HPV, HIV, HSV, HCV) was added and stirred for 3 h, and then dialyzed to remove excess antigen, and the final general metal nanovaccine platform LaMP-A-antigen was obtained. The RBD plasmid was extracted from the SARS-Cov-2-RBD-6His overexpression strain (Genechem) using EndoFree Mini Plasmid Kit II (REF: DP118-02, TianGen). SARS-CoV-2 Spike RBD Protein ELISA Kit was purchased from Abclonal (RK04135). His-tagged RBD expressed in the human embryonic kidney 293 cells (HEK293) cell line was purchased from Genscript. Influenza A H1N1 (A/swine/Jiangsu/J004/2018) Hemagglutinin / HA Protein (ECD, his-tag) was purchased from Sino Biological Inc (40649-V08H). HSV antigen $gB_{498–505HHHHHH}$ peptide (SSIEFARLHHHHHH), HIV antigen eOD-GT8 gp120 protein (residues AKFVAAWTLKAAAHHHHHH), HCV antigen HCV E2 envelope glycoprotein (residues 412 −423HHHHHH, QLINTNGSWHINHHHHHH) and HPV antigen peptide $E7_{HHHHHH49–57}$ (HHHHHHRAHYNIVTF) was synthesized by GenScript.

The contents of $Mn^{2+}$ and diABZI-2 in LaMP-A-antigen were determined by inductively coupled plasma optical emission spectrometer (ICP-OES) (iCAP7000 series) and microplate reader (excitation = 324 nm, emission = 436 nm), respectively. The concentration of RBD on LaMP-A-antigen was quantified using an ELISA kit (Cat: EKnCov-RBD-01, Frdbio). The morphology of LaMP-A-antigen was observed using transmission electron microscope (JEM-F200, JEOL). The size of the LaMP-A-antigen were measured using a Zetasizer (Nano ZS).

For the physical stability characterization of metal nanovaccine platforms, the LaMP-A-antigen were freeze-dried and treated with 20% FBS for 24 h, respectively. Changes of antigen and adjuvant content, particle size and PDI before and after LaMP-A-antigen treatment was detected.

For in vivo metal nanovaccine platform immune performance evaluation, 6–8 weeks old female BALB/c mouse were intranasally administered one dose of Mn-A-RBD, LaMP-A-antigen (RBD, Flu, HIV, HPV, HCV, HSV). On the 14th day, BALF, NPLF and serum were collected for subsequent antibody titer detection. All the animal procedures were approved by the Animal Experiment Ethics Committee at the Tianjin University (permit number: TJUE-2022–007).

### *Assessing the effect of metal ions and STING agonists on SARS-Cov-2 infection prevention*

For viral cell prophylactic assay, $2 \times 10^4$ A549/hACE2 cells (made and provided by Prof. Bin Zheng at Tianjin University) were added to a 96-well plate and incubated overnight. Metal ions ($CaCl_2$, $MgCl_2$, $CoCl_2$, $FeCl_2$, $FeCl_2$, $ZnCl_2$, $MnCl_2$, $NiCl_2$, KCl, $CuCl_2$) with or without diABAI-2 were pre-incubated for 20 h and then cells were infected with GFP-SARS-Cov-2 pseudovirus (MOI of 0.1, 0.3 and 0.6) (Genomeditech) for 20 h. The medium containing the virus was sucked away and washed twice with PBS, RAPI lysate was added to lyse the cells, and the fluorescence intensity of GFP was measured by a microplate reader.

For mouse immune activation effect assay, 6–8 weeks old female BALB/c mouse intranasally inhaled PBS, $Mn^{2+}$+RBD, diABZI-2 +RBD and $Mn^{2+}$+diABZI-2 +RBD with 20 μg $Mn^{2+}$, 15 μg diABZI-2 and 300 ng RBD on day 0 and day 7 respectively. On the 14th day, cytokines, antibody titer tests and neutralizing antibody titer tests were performed. All the animal procedures were approved by the Animal Experiment Ethics Committee at the Tianjin University (permit number: TJUE-2022–007).

### *RBD binding assay to A549/hACE2 cells*

RBD was labeled with FITC at room temperature. FITC DMSO solution was added dropwise to RBD sodium bicarbonate buffer (pH 9) for labeling ($n_{FITC}$:$n_{RBD}$ = 1.5:1), and then dialyzed three times with PBS to remove FITC. $3 \times 10^5$ A549 cells or A549/hACE2 cells were incubated with RBD-FITC, LaMP-RBD-FITC, LaMP-A-RBD-FITC (RBD, 0.5 μg $mL^{-1}$) on ice for 20 min. After incubation, cells were washed twice with ice-cold PBS. Cells were lysed with RAPI lysis buffer for 10 min on ice. The samples were placed in a 96-well plate, and the fluorescence signal of the FITC-labeled RBD was detected at the excitation/emission of 480/520 nm.

### *In vitro release of RBD, diABZI-2 and $Mn^{2+}$*

To study the RBD, diABZI-2 and $Mn^{2+}$ release at pH= 5.5 or 7.4, LaMP-A-RBD-FITC was put in dialysis bag (molecular weight cut off: 100000 Dalton) against 30 mL of 0.01 M phosphate buffer solution (pH=5.5 or 7.4). At pre-determined timepoints (20, 40, 60, 80, 120, 240 min). 0.2 mL of the buffer inside the dialysis bag was taken out for the quantification of RBD and diABZI-2 by microplate reader. 0.2 mL of the buffer inside the dialysis bag was taken out for the quantification of $Mn^{2+}$ by ICP-OES (iCAP7000 series).

### *LaMP-A-RBD internalization by APCs*

To visualize and quantify the cellular uptake of nanovaccine, RBD-FITC, LaMP-RBD-FITC and LaMP-A-RBD-FITC were incubated with

BMDCs. To study uptake kinetics, samples and cells were incubated for different times (t = 0.5, 1, 2, 4, 6, 8, 12 h). PBS and RAPI cell lysate were added to wash and lyse the cells respectively, and the fluorescence intensity (480/520 nm) was measured with a microplate reader. For confocal imaging, cells incubated for 6 h were washed three times with PBS. 50 nM lysosomal red fluorescent probe FluoLysoTM (UElandy, Suzhou, China) was incubated at 37 °C for 30 min for lysosome staining, 1 mL DAPI (Cat No.4072SES03; Yeasen, Shanghai, China) was added for 8 min at room temperature for nuclei staining, washed twice with PBS, and then used a confocal microscope imaging. To quantify cellular uptake, cells were harvested and washed twice with PBS. Fluorescence of FITC was analyzed using flow cytometry, and data were processed using FlowJo (v.10.5).

*Lyophilization and stability studies*

To test the effect of lyophilization, LaMP-RBD and LaMP-A-RBD solutions were lyophilized by freeze dryer, and enzyme-free sterile water was added for reconstitution. The redissolved samples were subjected to performance tests such as particle size test, RBD content and RBD uptake signal detection. In order to detect the effect of dry powder storage at room temperature on the performance of nanovaccine, freeze-dried LaMP-RBD and LaMP-A-RBD dry powders were stored at room temperature for 3 months, and enzyme-free sterile water was added for reconstitution. The redissolved samples were subjected to performance tests such as particle size test, RBD content and RBD uptake signal detection.

*In vitro assessment of BMDC maturation and STING activation*

The preparation method of BMDCs was described previously. In order to observe the activation of BMDCs by diABZI-2 and $Mn^{2+}$, $1 \times 10^6$ BMDCs were seeded in 6-well plates and incubated for 24 h with samples. Cell supernatants were collected for IFN β (Amoy Lunchangshuo Biotech, Co., Ltd.), IFN γ, TNF α cytokine ELISA detection (Solarbio, Beijing, China). The treated BMDCs were collected, APC anti mouse CD11c antibody, FITC anti-mouse CD40 antibody, PerCP-Cy5.5 anti-mouse CD86 antibody (Biolegend, California, America) were sequentially added and incubated on ice for 40 min. After incubation, cells were washed twice with PBS and resuspend in 500 μL PBS for future flow cytometry assay. Cells were analyzed for fluorescence using flow cytometry and data were processed using FlowJo (v.10.5).

*Western blot analysis*

BMDCs and A549/hACE2 cells incubated with samples for 6 h were collected, and RAPI lysate was added to lyse on ice for 10 min. The protein solution was collected by centrifugation at 10000 rcf for 10 min. Protein solution and protein loading buffer were boiled at 100 °C for 5–10 min. After cooling, the protein mixture solution was added to the wells of 12% SDS-PAGE gels. This process requires control that the total protein added to the 12% SDS-PAGE gels is the same. The voltage was 80 V for 30 min and 120 V for 2 h. When the protein bands were clearly separated on the SDS-PAGE gels, the power was turned off. SDS-PAGE gels were transferred to PVDF membranes (Solarbio, Beijing, China) at 220 mA on ice. After 2.5 h of transfer, the PVDF membrane was washed three times with TBST (Solarbio, Beijing, China), and 5% skimmed milk was added for blocking for 80 min. Primary antibodies were added and incubated overnight at 4 °C. Primary antibodies included phospho-NF-kappaB p65 (pS536) (Abways technology, Shanghai, China), NF-kappaB p65 (Abways technology, Shanghai, China), phospho-IRF3 (pS396) (Cell Signaling Technolog), IRF3 (Abways technology, Shanghai, China), phospho-TBK1 (pS172) (Abways technology, Shanghai, China), TBK1 (Abways technology, Shanghai, China). After washing three times with TBST, goat anti-rabbit IgG (Solarbio, Beijing, China) was added and incubated at room temperature for 1 h. Protein bands were visualized by chemiluminescence imaging with SHSP/substrate.

*Effect of activated macrophages on SARS-Cov-2 infection*

For macrophage activation experiments, RAW264.7 was incubated with PBS, Mn+A+RBD, LaMP-RBD and LaMP-A-RBD (500 ng $mL^{-1}$ RBD, 500 ng $mL^{-1}$ diABZI-2 and 12 μM $Mn^{2+}$) for 24 h. Cells were stained with PerCP-Cy5.5 anti-mouse CD86 antibody (Biolegend, California, America) for 40 min. Fluorescence of PerCP-Cy5.5 was analyzed using flow cytometry, and data were processed using FlowJo (v.10.5).

For uptake/degradation experiments, RAW264.7 was incubated with PBS, Mn+A+RBD, LaMP-RBD and LaMP-A-RBD (500 ng $mL^{-1}$ RBD, 500 ng $mL^{-1}$ diABZI-2 and 12 μM $Mn^{2+}$) for 24 h. SARS-Cov-2 pseudovirus (MOI of 0.1) was added to macrophages for 24 h (uptake period). The medium containing the SARS-Cov-2 pseudovirus was then replaced with fresh medium and cultured for another 24 h (degradation period). After the culture was completed, RAPI lysate was added, and GFP fluorescence was detected using a microplate reader.

For infection experiments, sample-incubated macrophages were incubated with SARS-Cov-2 pseudovirus (MOI of 0.1) for 24 h and then washed with PBS to remove extracellular virus. After an additional 24 h of incubation with fresh medium, cells were lysed for luciferase assessment.

For the killing experiment of infected cells, the activated macrophages with sample were added to HEK293/hACE2 cells infected with SARS-Cov-2 pseudovirus and incubated for 24 h, and the cell activity status was detected using the CCK8 kit.

*LaMP-A-RBD vaccination on mice without pseudovirus challenge with Alum+RBD control*

Female BALB/c mouse aged 6–8 weeks were intranasally administered two dose of PBS, RBD, Mn+A+RBD, LaMP-RBD, LaMP-A-RBD (contains 50 μg $Mn^{2+}$, 30 μg diABZI-2 and 500 ng RBD) and alhydrogel 2% aluminum gel (Cat: KX0210054, Biodragon)+RBD on day 0 and day 14, respectively (n = 5). On day 17, BALF, NPLF, blood, spleen and lymph nodes were collected for immunological analysis.

*Safety profile of LaMP-A-RBD*

Female BALB/c mouse aged 6–8 weeks were intranasally administered two dose of PBS, RBD, Mn+A+RBD, LaMP-RBD, LaMP-A-RBD (contains 50 μg $Mn^{2+}$, 30 μg diABZI-2 and 500 ng RBD) and alhydrogel 2% aluminum gel (Cat: KX0210054, Biodragon)+RBD on day 0 and day 14, respectively (n = 6). Blood and spleen were collected for serum biochemical analysis and weighed, respectively on day 17. During the administration period, changes in the body weight of the mice were detected.

*Hamster studies with pseudovirus*

Female Syrian golden hamsters aged 6–8 weeks were intranasally administered one dose of PBS, Mn+A+RBD, LaMP-RBD and LaMP-A-RBD (contains 50 μg $Mn^{2+}$, 30 μg diABZI-2 and 500 ng RBD). One week after inoculation, $1.0 \times 10^5$ TU SARS-CoV-2 (Genomeditech) was injected intranasally (30 μL per well). On the second day, ex vivo fluorescence imaging was performed on the lung tissue. On day 7, BALF, NPLF, blood, spleen and lymph nodes were collected for immunological analysis. For lung tissue immunoanalysis, lung tissue was collected, sectioned, and the sections were immunostained for analysis.

*IgG antibody titer assay*

RBD-specific IgG from serum was detected using ELISA. 100 μL of 3 μg $mL^{-1}$ RBD coating buffer (Solarbio, Beijing, China) was added to

the microtiter plate and incubated overnight at 4 °C. 200 μL of 2% (w/v) bovine serum albumin (BSA) wash solution was added for blocking wells at 37 °C for 1 h. After washing 3 times with washing solution, serial serum dilutions (1:50,1:100, 1:1000, 1:5000, 1:10,000, 1:50,000, 1:100,000, 1:200,000) were added. A 1:100 dilution of the control serum sample was added to the wells and incubated at room temperature (25 ± 2 °C) for 120 min. The titration plate was washed 3 times with washing solution, HRP-labeled anti-mouse IgG secondary antibody (100 μL per well) or HRP-labeled anti-hamster IgG secondary antibody (100 μL per well) was added and incubated for 45 min at room temperature (25 ± 2 °C). 100 μL of chromogenic substrate TMB was added to each well, and after 10–25 min of color development at room temperature (25 ± 2 °C) in the dark, 50 μL of stop solution was added. The order in which the stop solution is added should be the same as the order in which the chromogenic substrates are added. Within 5 min, use a microplate reader to detect the absorbance (450 nm). Endpoint titers for IgG were quantified by the reciprocal of the maximal serum dilution that exceeded the mean reading in the control group by more than twofold.

*IgA antibody titer assay*

RBD-specific sIgA from NPLF and BALF was detected using ELISA. To collect NPLF, the trachea was cut in the middle and the nasopharynx was flushed upwards from the cut with 200 μL PBS. The liquid was collected and washed twice, taking a total of 400 μL of washing liquid. To collect BALF, the trachea was exposed through a thoracotomy and transected at the top of the bronchial bifurcation. A needle was inserted into the trachea and the lungs were washed with 200 μL of PBS. The washing liquid was collected, and the washing was repeated three times, taking a total of 600 μL of washing liquid. 100 μL of 3 μg $mL^{-1}$ RBD coating buffer (Solarbio, Beijing, China) was added to the microtiter plate and incubated overnight at 4 °C. 200 μL of 2% (w/v) bovine serum albumin (BSA) wash solution was added for blocking wells at 37 °C for 1 h. Serial dilutions of NPLF and BALF (1:50, 1:100, 1:1000, 1:10,000, 1:50,000, 1:100,000, 1:1000,000) were added and incubated at room temperature for 120 min (the control sample was diluted 1:50). The titration plate was washed 3 times with washing solution, 100 μL of detection antibody working solution was added to the reaction well, and the plate was sealed at room temperature (25 ± 2 °C) for 60 min 100 μL of enzyme conjugate working solution was added to the reaction wells, incubated at 37 °C for 30 min, and washed 4 times. 100 μL of chromogenic substrate TMB was added to each well, and after 10–25 min of color development at room temperature (25 ± 2 °C) in the dark, 50 μL of stop solution was added. The order in which the stop solution is added should be the same as the order in which the chromogenic substrates are added. Within 5 min, use a microplate reader to detect the absorbance (450 nm). Endpoint titers of sIgA were quantified by the reciprocal of the maximal serum dilution that exceeded the mean reading by more than twofold in the control group.

*Cytokine measurement in BALF and splenocytes*

The collected BALF was ELISA tested for cytokines IFN β, IFN γ, TNF α and chemokine CXCL-10 according to the protocol provided by the manufacturer (Solarbio, Beijing, China). Splenocytes from each vaccinated mouse were cultured in 24-well plates ($1 \times 10^5$ cells per well) and restimulated with 5 μg $mL^{-1}$ RBD. After a 48 h incubation, antigen-specific cytokine amounts of IFN β, IL-12p70 and TNF α from culture medium were detected by ELISA using ELISA kits (Solarbio, Beijing, China) following the manufacturer's protocols. Splenocytes from each vaccinated mouse were challenged with 1 μg $mL^{-1}$ RBD and plated into ELISpot wells ($10^6$ per well) that were coated with anti-mouse IFN γ capture antibody. RBD-specific cells secreting IFN γ were measured using an ELISpot assay according to the manufacturers' protocol (Dakewe Biotech Co., Ltd, Shenzhen, China).

*Immune response of lung cells, spleen cells and lymphocytes*

Hamster BALF, lymph nodes and spleens were collected on day 7 after inoculation. BALF was centrifuged at 500 rcf for 5 min to collect lung cells. Lymph nodes and spleens were triturated and single cells collected through a 70 μm cell strainer in 50 mL tubes. Centrifuge at 500 rcf, add red blood cell lysate and lyse on ice for 5 min. Lymphocytes and splenocytes were collected by centrifugation at 500 rcf for 5 min. To detect cytokines in antigen-specific T cells, 1 μg $mL^{-1}$ of RBD was used to stimulate cells for 18 h. To evaluate dendritic cell maturation, cells were stained with APC anti mouse CD11c antibody, FITC anti-mouse CD40 antibody, PerCP-Cy5.5 anti-mouse CD86 antibody for 40 min on ice. To evaluate T cell activation, cells were stained with PE anti-mouse $CD4^+$ antibody, FITC anti-mouse $CD3^+$ antibody, PerCP/Cyanine5.5 anti-mouse CD45 antibody, and APC anti-mouse $CD8^+$ antibody for 40 min on ice. To evaluate NK cell activation, cells were stained with PerCP/Cyanine5.5 anti-mouse CD45 antibody, PE/Cyanine7 anti-mouse CD107a, APC anti-mouse CD49b (pan-NK cells), FITC anti-mouse $CD3^+$ antibody for 40 min on ice. To evaluate B cell activation, cells were stained with PE anti-mouse/human CD45R/B220 antibody, FITC anti-mouse CD40 antibody on ice for 40 min. To evaluate local immune memory, cells were stained with FITC anti-mouse $CD3^+$ antibody on ice, PE anti-mouse/human CD62L antibody, APC anti-mouse/human CD44 antibody for 40 min on ice. After staining, wash twice with PBS, use flow cytometer to analyze cell fluorescence, and use FlowJo (v.10.5) to process the data. All antibodies were purchased from Biolegend.

*Virus-based neutralizing antibody titer assay*

A549-hACE2 cells were seeded into 96-well plates overnight at a density of $1 \times 10^5$ cells/well. Serial dilutions of serum were incubated with virus for 30 min at room temperature, then 50 μL of different dilutions of virus and serum were added to each well after removal of 50 μL of medium, and cells were incubated for 48 h. Medium was removed from each well, 200 μL PBS was used to wash the cells, and then 200 μL luciferase substrate (Genomeditech) was added to measure luciferase activity.

*Immune memory assessment*

Mouse spleens were collected on day 30 after inoculation. Spleens were triturated and single cells were collected through a 70 μm cell strainer in 50 mL tubes, then subjected to centrifugation at 500 g and adding red blood cell lysates and sitting on ice for 5 min. Splenocytes were collected by centrifugation at 500 rcf for 5 min. To evaluate immune memory, cells were stained with FITC anti-mouse $CD3^+$ antibody on ice, PE anti-mouse/human CD62L antibody, APC anti-mouse/human CD44 antibody for 40 min on ice. After staining, samples were washed twice with PBS, following flow cytometry analysis. Data were processed by FlowJo (v.10.5). All antibodies were purchased from Biolegend.

*Statistical analysis*

Data were given as mean ± standard deviation (S.D.). Flow cytometry results were analyzed by FlowJo v10. NIR fluorescence images were analyzed by Living Image 4.3 software. The statistical significance of tumor growth and survival rate were calculated via the two-way ANOVA with Tukey's test and log-rank test, respectively. For multiple comparisons, a one-way analysis of variance (ANOVA) with Tukey's post hoc test was used. The level of significance was defined at $*p < 0.05$, $* *p < 0.01$, $* **p < 0.001$, $* ** *p < 0.0001$. All statistical analyses were performed using GraphPad Prism 8.0 software. All the data supporting the findings of this study are available within the article and its supplementary information files and from the corresponding author upon reasonable request. A reporting summary for this article is available as a Supplementary Information file.

## CRediT authorship contribution statement

**Lovell Jonathan F:** Writing – review & editing. **Zhang Yumiao:** Funding acquisition, Investigation, Methodology, Writing – original draft. **Liu Gengqi:** Software. **Zhang Chen:** Project administration, Resources. **Zheng Bin:** Resources. **Sun Boyang:** Software. **Qiu Qian:** Investigation, Methodology. **Li Jiexin:** Investigation, Methodology, Project administration, Software, Supervision, Visualization, Writing – original draft. **Zhang Jingyu:** Methodology, Project administration. **Ren He:** Methodology, Project administration.

## Declaration of Competing Interest

The authors declare that they have no known competing financial interests or personal relationships that could have appeared to influence the work reported in this paper.

## Data availability

Data will be made available on request.

## Acknowledgments

This work was supported by National Natural Science Foundation of China (22375144, 32071384), the National Key Research and Development Program (2021YFC2102300), Start-up Grant at Tianjin University and One-thousand Young Talent Program of China.

*Additional information*

Supplementary information is available in the online version of the paper.

## Appendix A. Supporting information

Supplementary data associated with this article can be found in the online version at doi:10.1016/j.nantod.2024.102156.

## References

[1] I. Mellman, G. Coukos, G. Dranoff, Nature 480 (2011) 480–489.
[2] C. Zhang, K. Pu, Chem. Soc. Rev. 49 (2020) 4234–4253.
[3] U. Sahin, Ö. Türeci, Science 359 (2018) 1355–1360.
[4] H. Ren, J. Li, J. Zhang, J. Liu, X. Yang, N. Zhang, Q. Qiu, D. Li, Y. Yu, X. Liu, J. F. Lovell, Y. Zhang, Small (2023).
[5] L. Dai, T. Zheng, K. Xu, Y. Han, L. Xu, E. Huang, Y. An, Y. Cheng, S. Li, M. Liu, Cell 182 (2020) 722–733, e711.
[6] J.X. Li, H. Ren, Y.M. Zhang, 454, Coord. Chem. Rev. (2022), 454.
[7] R.L. Coffman, A. Sher, R.A. Seder, Immunity 33 (2010) 492–503.
[8] W.C. Koff, D.R. Burton, P.R. Johnson, B.D. Walker, C.R. King, G.J. Nabel, R. Ahmed, M.K. Bhan, S.A. Plotkin, Science 340 (2013) 1232910.
[9] A.W. Purcell, J. McCluskey, J. Rossjohn, Nat. Rev. Drug Discov. 6 (2007) 404–414.
[10] J. Heuts, E.M. Varypataki, K. van der Maaden, S. Romeijn, J.W. Drijfhout, A.T. van Scheltinga, F. Ossendorp, W. Jiskoot, Pharm. Res. 35 (2018) 1–9.
[11] S.M. Bal, S. Hortensius, Z. Ding, W. Jiskoot, J.A. Bouwstra, Vaccine 29 (2011) 1045–1052.
[12] S. Eskandari, T. Guerin, I. Toth, R.J. Stephenson, Adv. Drug Deliv. Rev. 110 (2017) 169–187.
[13] N. Gong, Y. Zhang, X. Teng, Y. Wang, S. Huo, G. Qing, Q. Ni, X. Li, J. Wang, X. Ye, Nat. Nanotechnol. 15 (2020) 1053–1064.
[14] J. Xu, J. Lv, Q. Zhuang, Z. Yang, Z. Cao, L. Xu, P. Pei, C. Wang, H. Wu, Z. Dong, Nat. Nanotechnol. 15 (2020) 1043–1052.
[15] L.A. Canalle, D.W. Löwik, J.C. van Hest, Chem. Soc. Rev. 39 (2010) 329–353.
[16] K. Ulbrich, K. Hola, V. Subr, A. Bakandritsos, J. Tucek, R. Zboril, Chem. Rev. 116 (2016) 5338–5431.
[17] T.C. Pham, M.K. Jayasinghe, T.T. Pham, Y.Q. Yang, L.K. Wei, W.M. Usman, H. Chen, M. Pirisinu, J.H. Gong, S. Kim, B.Y. Peng, W.X. Wang, C. Chan, V. Ma, N. T.H. Nguyen, D. Kappei, X.H. Nguyen, W.L.C. Cho, J.H. Shi, M.T.N. Le, J. Extracell. Vesicles 10 (2021).
[18] P. Sapra, T. Allen, Prog. Lipid Res. 42 (2003) 439–462.
[19] W.R. Algar, D.E. Prasuhn, M.H. Stewart, T.L. Jennings, J.B. Blanco-Canosa, P. E. Dawson, I.L. Medintz, Bioconjugate Chem. 22 (2011) 825–858.
[20] A.C. Marques, P.J. Costa, S. Velho, M.H. Amaral, J. Control. Release 320 (2020) 180–200.
[21] D. Kirpotin, J.W. Park, K. Hong, S. Zalipsky, W.-L. Li, P. Carter, C.C. Benz, D. Papahadjopoulos, Biochemistry 36 (1997) 66–75.
[22] F.G. Liu, C.C. Ma, D.J. McClements, Y.X. Gao, Food Hydrocoll. 63 (2017) 625–634.
[23] L. Nobs, F. Buchegger, R. Gurny, E. Allémann, J. Pharm. Sci. 93 (2004) 1980–1992.
[24] P. Boisguerin, S. Deshayes, M.J. Gait, L. O'Donovan, C. Godfrey, C.A. Betts, M.J. A. Wood, B. Lebleu, Adv. Drug Deliv. Rev. 87 (2015) 52–67.
[25] E.L. Dane, A. Belessiotis-Richards, C. Backlund, J. Wang, K. Hidaka, L.E. Milling, S. Bhagchandani, M.B. Melo, S. Wu, N. Li, Nat. Mater. 21 (2022) 710–720.
[26] K. Lu, Q.P. Duan, L. Ma, D.X. Zhao, Bioconjugate Chem. 21 (2010) 187–202.
[27] D.S. Watson, F.C. Szoka Jr, Vaccine 27 (2009) 4672–4683.
[28] M.J. Roberts, M.D. Bentley, J.M. Harris, Adv. Drug Deliv. Rev. 54 (2002) 459–476.
[29] V. Platt, Z. Huang, L. Cao, M. Tiffany, K. Riviere, F.C. Szoka Jr, Bioconjugate Chem. 21 (2010) 892–902.
[30] R. Rüger, D. Müller, A. Fahr, R.E. Kontermann, J. Drug Target. 14 (2006) 576–582.
[31] S. Shao, J. Geng, H. Ah Yi, S. Gogia, S. Neelamegham, A. Jacobs, J.F. Lovell, Nat. Chem. 7 (2015) 438–446.
[32] W.-C. Huang, B. Deng, C. Lin, K.A. Carter, J. Geng, A. Razi, X. He, U. Chitgupi, J. Federizon, B. Sun, Nat. Nanotechnol. 13 (2018) 1174–1181.
[33] X. Sun, Y. Zhang, J. Li, K.S. Park, K. Han, X. Zhou, Y. Xu, J. Nam, J. Xu, X. Shi, Nat. Nanotechnol. 16 (2021) 1260–1270.
[34] J. Li, H. Ren, Q. Qiu, X. Yang, J. Zhang, C. Zhang, B. Sun, J.F. Lovell, Y. Zhang, ACS nano 16 (2022) 16909–16923.
[35] O.J. Wouters, K.C. Shadlen, M. Salcher-Konrad, A.J. Pollard, H.J. Larson, Y. Teerawattananon, M. Jit, Lancet 397 (2021) 1023–1034.
[36] Z. Wang, K.D. Popowski, D. Zhu, B.L. de Juan Abad, X. Wang, M. Liu, H. Lutz, N. De Naeyer, C.T. DeMarco, T.N. Denny, P.-U.C. Dinh, Z. Li, K. Cheng, Nat. Biomed. Eng. 6 (2022) 791–805.
[37] M.T. Mabrouk, K. Chiem, E. Rujas, W.-C. Huang, D. Jahagirdar, B. Quinn, M. Surendran Nair, R.H. Nissly, V.S. Cavener, N.R. Boyle, Sci. Adv. 7 (2021) eabj1476.
[38] M. Brown, F.P. Assen, A. Leithner, J. Abe, H. Schachner, G. Asfour, Z. Bago-Horvath, J. Stein, P. Uhrin, M. Sixt, Science 359 (2018) 1408–1411.
[39] S.M. Lewis, A. Williams, S.C. Eisenbarth, Sci. Immunol. 4 (2019) eaau6085.
[40] B.S. Berthon, L.M. Williams, E.J. Williams, L.G. Wood, Adv. Nutr. (2022).
[41] S.-A. Hwang, J.K. Actor, Int. Immunol. 21 (2009) 1185–1197.
[42] X. Li, Y. Cao, K. Luo, Y. Sun, J. Xiong, L. Wang, Z. Liu, J. Li, J. Ma, J. Ge, Nat. Catal. 2 (2019) 718–725.
[43] X. Li, Y. Cao, K. Luo, L. Zhang, Y. Bai, J. Xiong, R.N. Zare, J. Ge, Nat. Commun. 13 (2022) 2189.
[44] C. Wang, P.W. Horby, F.G. Hayden, G.F. Gao, lancet 395 (2020) 470–473.
[45] D. Mannar, J.W. Saville, X. Zhu, S.S. Srivastava, A.M. Berezuk, K.S. Tuttle, A. C. Marquez, I. Sekirov, S. Subramaniam, Science 375 (2022) 760–764.
[46] M. Li, M. Ferretti, B. Ying, H. Descamps, E. Lee, M. Dittmar, J.S. Lee, K. Whig, B. Kamalia, L. Dohnalová, Sci. Immunol. 6 (2021) eabi9007.
[47] F. Humphries, L. Shmuel-Galia, Z. Jiang, R. Wilson, P. Landis, S.-L. Ng, K.M. Parsi, R. Maehr, J. Cruz, A. Morales, Sci. Immunol. 6 (2021) eabi9002.
[48] J. Yang, W. Wang, Z. Chen, S. Lu, F. Yang, Z. Bi, L. Bao, F. Mo, X. Li, Y. Huang, Nature 586 (2020) 572–577.
[49] T. Yoji, O. Akira, S. Kinya, W. Masafumi, Y. Hiroshi, H. Norio, Am. J. Clin. Nutr. (2002) 112–118.
[50] C. Wang, Y. Guan, M. Lv, R. Zhang, Z. Guo, X. Wei, X. Du, J. Yang, T. Li, Y. Wan, Immunity, 675-687 48 (2018) e677.
[51] Dimitris, Thanos, and, Tom, Maniatis, Cell, (1995).
[52] P.Y.Jenny Ting, A. Duncan, Joseph, Lei, Yu, Science (2010).
[53] W. Liu, H.M. Reyes, J.F. Yang, Y. Li, K.M. Stewart, M.C. Basil, S.M. Lin, J. Katzen, E.E. Morrisey, S.R. Weiss, J. Virol. 95 (2021) e00490-00421.
[54] A. Park, A. Iwasaki, Cell Host Microbe 27 (2020).
[55] S. Spranger, D. Dai, B. Horton, T.F. Gajewski, Cancer cell, 711-723 31 (2017) e714.
[56] A.O. Hassan, N.M. Kafai, I.P. Dmitriev, J.M. Fox, M.S. Diamond, Cell (2020).
[57] G. Zhang, Y. Cong, F.-L. Liu, J. Sun, J. Zhang, G. Cao, L. Zhou, W. Yang, Q. Song, F. Wang, Nat. Nanotechnol. 17 (2022) 993–1003.
[58] A.O. Hassan, N.M. Kafai, I.P. Dmitriev, J.M. Fox, B.K. Smith, I.B. Harvey, R. E. Chen, E.S. Winkler, A.W. Wessel, J.B. Case, Cell, 169-184 183 (2020) e113.
[59] Q. Zhang, P. Bastard, Z. Liu, J. Le Pen, M. Moncada-Velez, J. Chen, M. Ogishi, I. K. Sabli, S. Hodeib, C. Korol, Science 370 (2020) eabd4570.
[60] R.W. Nelson, Y. Chen, O.L. Venezia, R.M. Majerus, D.S. Shin, M.C.- Collection, P. Team, M.N. Carrington, X.G. Yu, D.R. Wesemann, J.J. Moon, Sci. Immunol. 7 (2022) eabl9464.
[61] L.B. Ivashkiv, L.T. Donlin, Nat. Rev. Immunol. 14 (2014) 36–49.
[62] N. Vabret, G.J. Britton, C. Gruber, S. Hegde, J. Kim, M. Kuksin, R. Levantovsky, L. Malle, A. Moreira, M.D. Park, Immunity 52 (2020) 910–941.
[63] N. Lycke, Nat. Rev. Immunol. 12 (2012) 592–605.
[64] N.K. Björkström, B. Strunz, H.-G. Ljunggren, Nat. Rev. Immunol. 22 (2022) 112–123.
[65] C. Maucourant, I. Filipovic, A. Ponzetta, S. Aleman, M. Cornillet, L. Hertwig, B. Strunz, A. Lentini, B. Reinius, D. Brownlie, Sci. Immunol. 5 (2020) eabd6832.
[66] Q. Hammer, T. Rückert, C. Romagnani, Nat. Immunol. 19 (2018) 800–808.
[67] S. Madera, M. Rapp, M.A. Firth, J.N. Beilke, L.L. Lanier, J.C. Sun, J. Exp. Med. 213 (2016) 225–233.
[68] B. Zheng, W. Peng, M. Guo, M. Huang, Y. Gu, T. Wang, G. Ni, D. Ming, Chem. Eng. J. 418 (2021) 129392.